ANKRD5: a key component of the axoneme required for sperm motility and male fertility

Shuntai Yu[a,b,1], Guoliang Yin[d,1], Peng Jin[b], Weilin Zhang[b], Yingchao Tian[b], Xiaotong Xu[b], Tianyu Shao[a,b], Yushan Li [e], Fei Sun[d], Yun Zhu* [d], Fengchao Wang* [b,c]

[a] Academy for Advanced Interdisciplinary Studies, Peking University, Beijing 100871, China;
[b] National Institute of Biological Sciences (NIBS), Beijing 102206, China;
[c] Tsinghua Institute of Multidisciplinary Biomedical Research, Tsinghua University, Beijing 102206, China;
[d] Key Laboratory of Biomacromolecules, CAS Center for Excellence in Biomacromolecules, Institute of Biophysics, Chinese Academy of Sciences, Beijing 100101, China; University of Chinese Academy of Sciences, Beijing 100049, China;
[e] The School of Public Health, Xinxiang Medical University, Xinxiang 453003, China.
[1] Shuntai Yu and Guoliang Yin contributed equally to this work

ORCID Identifiers:
Shuntai Yu: [https://orcid.org/0009-0001-7249-1502]
Guoliang Yin: [https://orcid.org/0000-0002-2156-8258]
Fei Sun: [https://orcid.org/0000-0002-0351-5144]
Yun Zhu: [https://orcid.org/0000-0001-9382-8592]
Fengchao Wang: [https://orcid.org/0000-0003-4252-5406]

Corresponding Authors:
* Yun Zhu, 15 Datun Road, Chaoyang District, Beijing, 100101, China. Phone: +86-(0)10-64888582, Email: zhuyun@ibp.ac.cn
* Fengchao Wang, 7 Science Park Road ZGC Life Science Park, Beijing, 102206, China. Phone: +86-(0)10-80726688-8585, Email: wangfengchao@nibs.ac.cn

Author Contributions: Fengchao Wang, Yun Zhu ,Fei Sun, Shuntai Yu, and Guoliang Yin designed research; Shuntai Yu, Guoliang Yin, Peng Jin, Weilin Zhang, Yingchao Tian, Xiaotong Xu, Tianyu Shao, and Yushan Li performed research; Yun Zhu ,Fei Sun, Guoliang Yin contributed Cryo-ET expertise; Shuntai Yu, Guoliang Yin, and Fengchao Wang, Yun Zhu ,Fei Sun analyzed data; and Shuntai Yu, Guoliang Yin, and Fengchao Wang wrote the paper.

Competing Interest Statement: The authors declare no competing interest.

Classification: Biological Sciences (Developmental Biology)

Keywords: sperm motility; ANKRD5; axoneme; N-DRC; male infertility

This PDF file includes:

Main Text
Figures 1 to 7
Figure S1 to S6
Tables 1

Abstract

Sperm motility is crucial for male reproduction and relies on the structural integrity of the sperm axoneme, which has a "9+2" microtubule configuration. This structure includes nine outer microtubule doublets that house various macromolecular complexes. The nexin-dynein regulatory complex (N-DRC) forms a crossbridge between the outer microtubule doublets, stabilizing them and facilitates sperm tail bending. Our investigation of ANKRD5, which is highly expressed in the sperm axoneme, reveals its interaction with TCTE1 and DRC4/GAS8, both key components of the N-DRC. The components of the N-DRC are often vital for sperm motility. ANKRD5$^{-/-}$ mice exhibited reduced sperm motility and male infertility; however transmission electron microscopy and cryoelectron tomography showed no significant alterations in microtubule doublets. Moreover, ANKRD5 deficiency did not affect ATP levels, and its interactions with TCTE1 and DRC4/GAS8 were found to be independent of calcium regulation. These findings establish that ANKRD5 is critical for maintaining axoneme stability, which is important for sperm motility.

Significance Statement

Male infertility affects 8%-12% of men globally, with defects in sperm motility accounting for 40%-50% of these cases. The axoneme, serving as the sperm's motor apparatus, features a 9+2 microtubule arrangement, with the nexin-dynein regulatory complex (N-DRC) providing essential structural support between outer microtubule doublets. Understanding the synergistic relationship between the N-DRC's structure and its protein composition is crucial for advancing male reproductive biology. In this study, we identify the protein ANKRD5 as a component of the axoneme that can interact with N-DRC components, which is crucial for sperm motility. This discovery enhances our understanding of sperm motility mechanisms and suggests potential targets for male contraceptive development.

Main Text

Introduction

The interaction between sperm and egg, leading to embryo formation, is fundamental for life reproduction and species continuity (1). Male infertility impacts 8%-12% of the global male population, with sperm motility defects contributing to 40%-50% of these cases (2, 3) Fertilization relies on successful spermatogenesis and normal sperm motility (4), which occurs in the testes. Mammalian sperm gain motility and fertilization capabilities when they pass through the epididymis (5). The maturation of sperm in the epididymis is necessary for the production of fertile sperm. Asthenospermia caused by poor sperm motility is the main symptom of clinical infertility, yet its precise pathogenesis remains largely unclear (6). Individuals with poorly motile or immobile sperm are typically infertile unless advanced assisted reproductive techniques, such as gamete intrafallopian transfer (GIFT), in vitro fertilization (IVF), or intracytoplasmic sperm injection (ICSI), are employed (7). However, these common assisted reproductive technologies may pass genetic defects to offspring. A more comprehensive understanding of the molecular mechanisms underlying sperm motility could lead to more effective clinical interventions for hypofertility caused by asthenospermia. Rather than bypassing the issue with ICSI, infertility from poor sperm motility could potentially be treated or even cured through stimulation of specific signaling pathways or gene therapy.

Sperm motility is driven by flagellar beating. The flagellum consists of three main parts: the midpiece, principal piece, and endpiece (8). These three parts share a common central axoneme composed of approximately 250 proteins that are major components of the flagellum (9). The axoneme exhibits a 9+2 microtubule doublet structure, with the N-DRC forming cross-bridges between the outer microtubule doublets (10). Both the structure and molecular composition of N-DRC are evolutionarily conserved and play a central role in regulating sperm motility (11-13). The N-DRC is a large, complex structure with a molecular weight of approximately 1.5 MDa and can be

divided into two regions: the linker and the base plate (12-14). The N-DRC is a large, complex structure with a molecular weight of approximately 1.5 MDa and can be divided into two regions: the linker and the base plate (14-16). Additionally, the N-DRC interacts with the outer dynein arms (ODA) via outer-inner dynein (OID) linkers, functioning as a regulatory component for both ODA and inner dynein arms (IDA) (17).

It was previously believed that N-DRC comprised 11 protein components (13, 18). However, integrated modeling combined with in situ cross-linking mass spectrometry revealed the existence of CCDC153 (DRC12), which is cross-linked with DRC1 (19). In situ cryoelectron tomography (cryo-ET) has further advanced understanding of the N-DRC architecture in Chlamydomonas, demonstrating that DRC1, DRC2/CCDC65, and DRC4/GAS8 constitute its core framework (16). Additionally, proteins DRC3/5/6/7/8/11 associate with this framework and engage with other axonemal complexes (20). Biochemical experiments corroborate these findings and support this model. The integrity of the N-DRC structure is crucial for flagellar movements, and mutations of N-DRC subunits may lead to defects in flagellar movement (15, 21-23). The N-DRC functions between the doublet microtubules (DMTs) to convert sliding into axonemal bending motion by restricting the relative sliding of outer microtubule doublets (24-26). Additionally, the formation of the N-DRC necessitates the coordination among various subunits. Mutations in three specific subunits—DRC1, DRC2/CCDC65, and DRC4/GAS8—have been previously associated with human ciliary motility disorders leading to primary ciliary dyskinesia (PCD) (12, 27). Knockout or mutation of *Lrrc48 (Drc3)* (28), *Tcte1 (Drc5)* (29), *Drc7* (30), and *Iqcg (Drc9)* (31) in mouse has been shown to cause male infertility. Our findings indicate that ANKRD5 (Ankyrin repeat domain 5, ANKRD5, ANK5, ANKEF1) could interact with N-DRC structure, serving as an auxiliary element to facilitate collaboration among DRC members. The absence of ANKRD5 results in diminished sperm motility and subsequent male infertility.

Results

Ankrd5 is critical for male fertility.

The auxiliary factors required for the N-DRC structure to function effectively have not been fully elucidated. As an important structural component of the axoneme, the functionality of the N-DRC relies on protein interactions. The ANK domain is one of the crucial domains for protein interactions. Based on an analysis of the NCBI database and relevant single-cell sequencing data, *Ankrd5* expression is predominantly localized to the male reproductive system, with a relatively high expression specificity (32). However, the impact of ANKRD5 on the functionality of the N-DRC remains unclear. In mice, ANKRD5 is a protein comprising 775 amino acids with a molecular weight of 86.9 kDa. Comparative analysis of the ANKRD5 protein sequence across various species revealed that it is relatively conserved (Fig. S1A). Sequence alignment using Clustal Omega demonstrated an 86% similarity between ANKRD5 sequences in mice and humans (Fig. S1B), suggesting that studying ANKRD5 in mice has significant translational relevance for human applications. We further confirmed this tissue-specific expression in mice through qPCR, demonstrating that *Ankrd5* was highly expressed in the testes, with no detectable levels in the brain, liver, spleen, kidney, ovary, intestine, or stomach (Fig. 1A). Further investigation into the temporal expression of *Ankrd5* in mouse testes indicated that its expression begins on postnatal day 21 and reaches peak levels by postnatal day 35 (Fig. 1B), which coincides with the emergence of mature sperm.

To explore the biological function of *Ankrd5* in vivo, we generated an *Ankrd5* knockout mouse line (*Ankrd5*$^{-/-}$) on a C57BL/6J background by targeting exons 4 and 7 using CRISPR/Cas9. The knockout was confirmed at the gene level (Fig. 1C). Fertility tests showed that *Ankrd5*$^{-/-}$ males were able to mate with wild-type females but did not produce any offspring (Table 1). These results indicated that *Ankrd5* is essential for male fertility. Since there were no significant differences in litter size (Table 1) and spermatogenesis between WT and het male mice (Fig. 1 D and E), we used

het as the experimental control. No significant differences were observed in spermatogenesis between *Ankrd5*$^{-/-}$ and control mice (Fig. 1 DE and G). The testis-to-body weight ratio and the morphology of the reproductive system in *Ankrd5*$^{-/-}$ mice were also normal (Fig. 1F and S1C-D). Histological analysis of hematoxylin-eosin-stained paraffin sections further confirmed that the structure and cellular composition of the seminiferous tubules were comparable between *Ankrd5*$^{-/-}$ and control mice (Fig. 1G). These results indicated that the infertility phenotype in *Ankrd5*$^{-/-}$ mice was not a result of defective spermatogenesis.

Due to decreased sperm motility, *Ankrd5* null sperm were unable to penetrate the zona pellucida

To investigate the cause of infertility in *Ankrd5* knockout mice, we performed in vitro fertilization (IVF) experiments. control sperm successfully fertilized both cumulus-intact eggs and cumulus-free eggs (Fig. 2A and B). In contrast, *Ankrd5* null sperm failed to fertilize the cumulus-intact eggs despite normal binding to the zona pellucida (ZP) (Fig. 2 A and D). However, *Ankrd5* null sperm were able to fertilize zona pellucida-free eggs and develop to blastocyst (Fig. 2C). These results indicate that the infertility observed in *Ankrd5* null sperm is primarily due to the sperm's inability to penetrate the zona pellucida. Sperm penetration through the cumulus-oocyte complex (COC) is influenced by two key factors: the acrosome reaction and sperm motility (33). Notably, *Ankrd5* null sperm exhibit a normal acrosome reaction when stimulated with calcium ionophore A23187 (Fig. 2 E and F), suggesting that the reproductive defects are not attributable to an acrosome reaction deficiency.

Sperm motility is critical for penetrating the cumulus oophorus and zona pellucida, which are softened by the acrosome reaction. Computer-assisted sperm analysis (CASA) revealed significant reductions in curvilinear velocity (VCL), average path velocity (VAP), and straight line velocity (VSL) in *Ankrd5* null sperm compared to controls (Fig. 3A). Additionally, forward progression parameters such as straightness (STR) and linearity (LIN) were also diminished (Fig. 3A). Sperm were categorized into four motility grades: rapid, medium, slow, and static. Significant differences were observed in the distribution of rapid, slow, and static grades, while no significant difference was noted in the medium grade (Fig. 3B). The proportions of total and progressive motility decreased with the loss of *Ankrd5* function (Fig. 3C). Furthermore, the tracking of sperm trajectories over time revealed that *Ankr5*$^{-}$ null sperm exhibited lower motility compared to controls (Fig. 3D). Moreover, sperm migration experiments revealed a significantly lower presence of *Ankrd5* null sperm in the female uterus and oviducts six hours after mating (Fig. 3E-G), further supporting the observed motility defects. These findings suggest that the reduced motility of *Ankrd5* null sperm compromised their ability to penetrate the outer layers of the egg.

ANKRD5 is primarily localized in the sperm axoneme

To explore the biological function of ANKRD5, we generated *Ankrd5-FLAG* mice by inserting a FLAG tag at the C-terminus using homologous recombination (Fig. S2A). Tissue sectioning and hematoxylin and eosin staining were performed to evaluate the epididymal structure and cellular composition in *Ankrd5-FLAG* male mice compared to controls (Fig. S2 B and C). The results revealed that the epididymis exhibited a normal structure, and the reproductive capabilities of *Ankrd5-FLAG* mice were intact, indicating that FLAG insertion did not impair the biological function of ANKRD5. Western blot analysis was employed to examine ANKRD5 protein expression across multiple organs and tissues, including liver, lung, kidney, heart, testis, spleen, brain, small intestine, skin, and sperm. The data revealed that ANKRD5 was predominantly expressed in mouse sperm (Fig. 4A), with lower expression levels in the testis. To further investigate ANKRD5 localization within sperm, we subjected sperm to repeated freeze-thaw cycles followed by density gradient centrifugation to separate the head and tail. Western blot analysis confirmed that ANKRD5 was primarily localized in the tail (Fig. 4B).

The sperm tail comprises three sections: midpiece, principal piece, and end piece. Immunofluorescence staining of adult mouse sperm revealed that ANKRD5 was primarily localized in the midpiece (Fig. 4C). As reported in previous studies, proteins from different regions of the

sperm tail can be extracted with varying lysate intensities (29, 34, 35). To determine the precise localization of ANKRD5, we used specific markers, including BASIGIN, Acetylated Tubulin, and AKAP4, representing the Triton X-100 soluble, SDS soluble, and SDS resistant fractions, respectively. These three fractions contain, respectively, membrane-associated and cytosolic proteins, axonemal proteins, as well as fibrous sheath and outer dense fiber proteins (29, 34, 35). The results indicated that ANKRD5 was primarily located in the SDS soluble fraction, suggesting its association with the sperm axoneme (Fig. 4D). These findings suggest that the infertility associated with the reduced motility in *Ankrd5* null sperm may be linked to impaired axoneme function in the sperm tail.

ANKRD5 interacts with axoneme N-DRC components

In order to explore the function of ANKRD5 in the axoneme, we explored the interactome of ANKRD5 using LC-MS (Fig. 5A). We identified the presence of several N-DRC components, including TCTE1, DRC3/LRRC48, DRC7/CCDC135, and DRC4/GAS8, with TCTE1 ranking highly in the mass spectrum (Fig. 5A). TEM analysis indicates that *Tcte1* null sperm maintain a normal DMT structure yet exhibit reduced motility (29), a phenotype similarly observed in ANKRD5 knockout sperm. ANKRD5 was identified in the TCTE1 mass spectrum with a high ranking, but their interaction had not been experimentally validated before our study (29). We performed immunoprecipitation in 293T cells and validated protein interactions with 11 DRC components, except for DRC6, which failed to express (Fig. 5 B and C, Fig. S3 A and B). Our results confirmed that ANKRD5 interacts with TCTE1 and DRC4/GAS8, but no interaction with other DRC components (Fig. 5 B and C, Fig. S3 A and B). ANKRD5 consists of two ANK domains and one EF-hand domain. The ANK domain is classic mediator of protein interactions, and the EF-hand domain typically functions as a calcium sensor; however, approximately one-third of EF-hand domains lack calcium-binding capability (36). Through protein truncation experiments, we found that the ANK2 domain mediates the interaction between ANKRD5 and TCTE1 (Fig. 5E). But, the interaction between ANKRD5 and DRC4/GAS8 requires the presence of both the ANK1 and ANK2 domains (Fig. 5F). The EF-Hand domain is not necessary for the interaction between ANKRD5 and TCTE1 or DRC4/GAS8. Western blot results indicated that calcium ions do not affect the interaction between ANKRD5 and DRC4/GAS8 or TCTE1 (Fig. 5G).

As is well known, energy metabolism is crucial for sperm motility. The TCTE1 null sperm showed a decrease in ATP levels (29). The loss of ANKRD5 does not change ATP levels in the sperm (Fig. 6E). This result indicates that ANKRD5 can interact with N-DRC components without impacting energy metabolism. The mitochondrial sheath is located in the midpiece of sperm, where mitochondria play a key role in energy production and serve as a significant source of reactive oxygen species (ROS) (37, 38). A balanced level of ROS is crucial for several essential sperm functions, including motility, capacitation, the acrosome reaction, fertilization, and hyperactivation (39-41). Mitochondrial membrane potential (MMP) is correlated with sperm motility (42). Decreased MMP (depolarization) indicates mitochondrial dysfunction, while increased MMP (hyperpolarization) leads to excess ROS. MMP in spermatozoa was assessed using TMRM staining and fluorescence imaging (Fig. S4 A and B). ROS levels were measured using DCFH-DA staining, followed by fluorescence imaging (Fig. S4 C and D). We found no significant differences between *Ankrd5* null sperm and control. Thus, ANKRD5 deficiency did not significantly affect sperm ATP levels and mitochondrial function.

The knockout of *Ankrd5* does not affect the overall structure of DMT

The absence of certain DRC components has been shown to alter the expression of other N-DRC proteins. For instance, DRC2/3/4 expression is reduced in DRC1 mutant mice (27), while DRC1/3/5/11 expression is downregulated in Chlamydomonas DRC2 mutants (12). To assess the impact of ANKRD5 deletion on sperm protein composition, we conducted quantitative proteomics using 4D-SmartDIA. Mass spectrometry identified 4,880 quantifiable proteins, of which 126 were differentially expressed (1.5 fold change), including 10 upregulated and 116 downregulated proteins (Fig. 6 A and B). DRC components were not included in the differentially expressed proteins list. In order to better understand the expression changes of these key proteins, the

intensity data of DRC components were extracted and normalized, then performed the T-test. Due to technical limitations, DRC6 and DRC12 were not detected. However, the analysis revealed a significant difference in DRC11(IQCA1). As no effective commercial antibody was available, DRC11 was not tested using Western blottign (Fig.6C). TCTE1 deficiency has been associated with abnormalities in glycolysis, leading to decreased ATP levels and reduced sperm motility (29). We conducted a Gene Set Enrichment Analysis (GSEA) focusing on this term, but the results were not significant, which is consistent with our ATP measurement results (Fig.6D and E).

The sperm axoneme follows a 9+2 structural arrangement, composed of nine outer microtubule doublets surrounding two central microtubules. Structural defects in this 9+2 arrangement may impair motility, but transmission electron microscopy of the sperm flagellum did not reveal any structural defects in *Ankrd5*$^{-/-}$ mice (Fig. 4E). To further explore the effects of *Ankrd5* knockout on each component of mouse sperm axoneme, we collected about 160 tilt series of *Ankrd5* null sperm axoneme using cryo-focused ion beam (cryo-FIB) and cryo-electron tomography (cryo-ET). Data pre-processing and reconstruction were performed by Warp and AreTOMO (43-45) (Fig. S5A). In the original tomograms obtained, we found that the overall "9+2" structure of sperm axonemes remained intact regardless of side view or top view, and there was no significant difference from that of WT mouse sperm axonemes (Fig. 7A) (46), which was similar to TEM results. Among the 89 tomograms with good quality, we carried out manual particle selection of DMT fiber and applied RELION, M, and other software to carry out sub-tomogram average analysis (STA) (47-49). The 8nm-repeats DMT structure of *Ankrd5* null sperm axoneme with a resolution of 24 Å was obtained (Fig. S5B and Fig. S6), and the overall structure of its A and B tubes was complete (Fig. 7 B and D). We compared the DMT density map of *Ankrd5*$^{-/-}$ mouse sperm with that of WT mouse sperm (EMD-35210/35211) and found that there was no significant difference between them, except for some difference in density between A05 of tube A and B09 and B10 of tube B (Fig. 7C and D) (46). This may be due to the difference between the density maps of 8nm-repeats DMT and 16nm-repeats DMT itself. The known 16nm-repeats mouse sperm DMT model was fitted into two density maps, and all 16nm-repeats MIPs including tubulins could be well fitted. We must emphasize that although there appears to be no significant difference on overall DMT structure between the wild-type and *Ankrd5* null sperm, we observed notable sample heterogeneity when manually selecting particles for *Ankrd5* null sperm. This resulted in a significantly reduced quantity of particles with the 96 nm periodicity, which is distinctly different from the WT results. We were able to detect the N-DRC structure in WT sperm, but we failed to find the density of N-DRC adjacent to RS3 in *Ankrd5* null sperm (50) (Fig. S6).

Discussion

During natural fertilization, males could ejaculate millions of sperm, but most are expelled by contractions in the female reproductive tract. Freshly ejaculate sperm exhibit activate movements, and only a few hundred activated sperm reach the isthmus of the fallopian tube, where they attach to the mucosal epithelium to form a sperm reservoir, remaining dormant until ovulation (51). Then, upon release from the reservoir, sperm transition to a hyperactivated state to approach the egg. Activation sperm exhibit symmetrical flagellar oscillations and swim along near-linear trajectories, whereas hyperactivated sperm display high-amplitude, asymmetrical flagellar oscillations (52). Activation is the prerequisite for hyperactivation. The outer layer of the COC is rich in hyaluronic acid, which gives it highly viscoelastic (53). Acrosome reaction releases hyaluronidase, which softens the cumulus cell layer and facilitate sperm-egg interaction. Sperm motility plays an important role in penetrate the COC (33). It has been reported that vole sperm can penetrate the zona pellucida of mice and hamsters without acrosome reaction, underscoring the importance of mechanical forces in sperm penetration of the COC (54).

N-DRC is critical for sperm motility. The auxiliary factors required for the N-DRC structure to function effectively have not been fully elucidated. As an important structural component of the axoneme, the functionality of the N-DRC relies on protein interactions. ANKRD5 is evolutionarily conserved and features a helix-turn-helix repeat structure known as the ANK domain, which is a

common motif involved in protein-protein interactions. (55). Given the high expression of ANKRD5 in the testes and its presence in the LC-MS results of TCTE1, we are concerned about the potential synergistic role of ANKRD5 in the function of N-DRC. Previous studies have found that ANKRD5 plays a critical role in cell adhesion and protrusion, contributing to the normal formation of the Xenopus gastrula (56). Furthermore, *Ankrd5* has been identified as differentially expressed in normozoospermic and asthenozoospermic males (57).

Ankrd5$^{-/-}$ male mice exhibit normal spermatogenesis and are able to mate and produce mating plugs, but failed to produce offspring. Histological and morphological of the *Ankrd5*$^{-/-}$ appeared normal. The IVF results found that *Ankrd5* null sperm could penetrate cumulus cells, but they could not fertilize cumulus-intact eggs, even after granulosa cell were removed. Interestingly, zona pellucida free eggs were successfully fertilized, and the resulting embryos developed normally to the blastocyst stage. Our findings indicate that the absence of ANKRD5 results in male infertility due to the inability of *Ankrd5* null sperm to penetrate the zona pellucida during fertilization. Acrosome reaction and sperm motility is important for sperm to penetrate the ZP. We used A23187 to induce the acrosome reaction and found that *Ankrd5* null sperm exhibited normal acrosome reaction. However, CASA revealed reduced motility in *Ankrd5* null sperm, suggesting that their inability to penetrate the zona pellucida is linked to abnormal motility rather than defective acrosome function. Our sperm migration results support this conclusion.

The sperm axoneme, a 9+2 motor apparatus, is critical for motility. Dynein arms on A-tubules hydrolyze ATP to "walk" along adjacent B-tubules, driving microtubule sliding. The N-DRC converts this sliding into flagellar bending (24, 25). Mass spectrometry identified several N-DRC members, including DRC5/TCTE1, DRC3/LRRC48, DRC7/CCDC135, and DRC4/GAS8. ANKRD5 knockout sperm shows a phenotype similar to TCTE1 knockout sperm, suggesting ANKRD5 may have a similar role to TCTE1. *Drc3/Lrrk48* knockout mice can grow up to adult and are capable of mating, but they are unable to produce offspring (28). In chlamydomonas, *Drc3/Lrrc48* mutations cause flagellar motility defects (11). *Drc7/Ccdc135* knockout mice exhibit short-tailed sperm, leading to male infertility (30), while DRC4/GAS8 (58) is associated with PCD in humans. Immunoprecipitation validated the mass spectrometry results, and GSEA analysis along with ATP measurements confirmed that ANKRD5 deficiency does not impact energy metabolism. Thus, ANKRD5 likely acts as a structural component aiding N-DRC function without involvement in metabolism.

TEM analysis showed no significant difference in the axoneme structure between wild-type and *Ankrd5* null sperm, which may be due to the imaging technique's low resolution. We therefore aim to use Cryo-ET to compare their electron density. Tilt series of *Ankrd5* null sperm axonemes were collected by cryo-focused ion beam and cryo-electron tomography, and 160 tomograms were obtained by data pre-processing and reconstruction. However, in the process of manual selection of DMT fibers, we found that they were not as smooth as WT particles. This suggests that the knockout of *Ankrd5* may affect the structural stability of the axoneme, although no significant difference was found in tomograms. We obtained the 8nm-repeats DMT *in situ* structure of 24 Å *Ankrd5* null sperm axonemes by sub-tomogram averaging. On the whole, although there is no obvious difference from the DMT density map of WT, there is a little deformation of tubulin, which does not indicate that DMT is damaged. When classifying 96nm-repeats DMT, we obtained a density similar to RS3, indicating that axoneme components such as DMT, CPC, and RS were not significantly affected, but we failed to obtain the corresponding density of N-DRC, which may be the average result of axoneme motility disturbance caused by decreased sperm motility. It is not clear if N-DRC was damaged.

Asthenospermia, characterized by reduced sperm motility, is a major cause of clinical infertility, yet its precise pathogenesis remains unclear. Investigating the infertility observed in *Ankrd5*$^{-/-}$ mice may provide insights into the underlying causes of asthenospermia. While current birth control pills primarily target women, they can have adverse side effects such as dizziness, chest pain, decreased libido, and vision impairment. As a result, the development of a male contraceptive has become an urgent priority. Currently, no oral contraceptive is available for men, but our study offers

new perspectives for male contraceptive research. ANKRD5 may represent a promising target for the development of such contraceptives.

Materials and Methods

Animals.

All animal experiments were approved by the Animal Care and Use Committee of the Beijing Institute of Biological Sciences. C57BL/6 wild-type mouse were obtained from the SPF Breeding Facility of the Animal Center of the Beijing Institute of Biological Sciences. They were maintained on a 12-hour light-dark cycle (from 7:00 am to 7:00 pm) and provided with adequate food and drinking water.

Real-time Quantitative PCR.

RNA was extracted from specific tissues using Trizol (Invitrogen, 15596026). The tissues were thoroughly homogenized with a drill and left at room temperature for 5 minutes to completely lyse the tissue. Chloroform was added and vigorously mixed for 15 seconds. Then, the mixture was incubated at room temperature for 3 minutes and centrifuged at 12,000× g for 15 minutes at 4℃ (repeated twice). Isopropanol was added to the supernatant, gently inverted several times, and left at room temperature for 10 minutes. After centrifugation at 12,000 × g for 10 minutes at 4 °C, the solution was discarded. The pellet was mixed with 75% ethanol, vortexed, and centrifuged at 7500 × g for 5 minutes at 4 °C. The supernatant was discarded, and the pellet was dried for 3-5 minutes. Water was added to resuspend the RNA, which was then shaken well at 65°C for 3 minutes and immediately placed on ice. RNA was reverse-transcribed into cDNA using a kit (TaKaRa, RR047A) according to the instruction manual. The qPCR system was set up following the recommended protocol of the kit (TaKaRa, DRR420A), and the relative expression of *Ankrd5* was calculated using *Gapdh* as the internal reference.

Generation of *Ankrd5*-deficient *and* ANKRD5-FLAG Mouse.

Female wild-type mouse aged between 4 to 6 weeks were intraperitoneally injected with PMSG to promote follicle development. Subsequently, they were injected with hCG (10 IU/mouse) at a 47-hour interval. After mating with male mouse, fertilized eggs were collected as recipients. *Ankrd5*$^{-/-}$ mouse were generated by co-injecting Cas9 mRNA and sgRNA1, sgRNA2 into the fertilized eggs. The sequences of sgRNA1 and sgRNA2 are as follows: sgRNA1: 5 'cctgcccactaagcggcactatc 3', sgRNA2: cctctcatgatagcgtgtgccag. ANKRD5-FLAG mouse were created by injecting Cas9 mRNA, gRNA, and ANKRD5-FLAG plasmid into fertilized eggs. Please refer to Fig. 1.C and Fig.S2A for specific strategies.

Histological Analysis.

The testes and epididymis tissues were dissected and placed in Davidson's Fluid (Formaldehyde: Ethanol: Glacial acetic acid: H2O = 6:3:1:10). After fixation at 4℃ for 2 hours, the testis was sliced using a blade, and the tissue sample was fully immersed in the fixing solution at 4 °C overnight. The tissue was then dehydrated, and 5μm thick sections were prepared. The sections were spread with warm water at 42 °C and baked overnight at 42 °C. Subsequently, the sections were dewaxed and stained with hematoxylin and eosin (H&E) following standard protocols. Images were captured using an Olympus VS120 microscope.

In vivo fertilization experiments.

Female wild-type mouse aged 4-6 weeks were intraperitoneally injected with PMSG to induce follicular development, followed by an injection of human chorionic gonadotropin hCG (10IU/mouse) after a 47-hour interval. After mating with male mouse, fertilized eggs were collected from the female mouse. The oocytes were treated with hyaluronidase (Sigma-Aldrich, H3757) for 10 minutes

to remove cumulus cells or with Tyrode's salt solution (Sigma-Aldrich, T1788) for 1 minute to remove the zona pellucida. Sperm were added to TYH droplets containing cumulus-free or ZP-free oocytes, with a final sperm concentration of $1x10^6$ sperm/ml. For intact egg testing, the final sperm concentration was $1x10^4$ sperm/ml. After co-incubation at 37 °C with 5% CO2, the number of two-cell stage embryos was determined after 36 hours, and the number of blastocysts was determined after 3.5 days.

Acrosome reaction analyses.

Sperm was placed in HTF medium under conditions of 37 °C and 5% CO2 for 30 min. Part of sperm were incubated with A23187 (21186-5MG-F) at a final concentration of 10 μmol/L, and the other sperm were incubated with DMSO, incubated for 50min, and then fixed with 4% PFA at room temperature for 30min and spread on the glass. The slides were stained with Coomassie brilliant blue solution (0.22% Coomassie Blue R-250, 50% methanol, 10% glacial acetic acid, 40% water) for 10 minutes and washed with water to remove floating color. Images were acquired using an Olympus VS120 microscope. Each scan included five regions, with a count of 100 sperm per region.

Sperm motility analyses.

Sperm was placed in HTF medium under conditions of 37 °C and 5% CO2 for 1 hour. After discarding the cauda tissue, sperm motility was analyzed using the CASA system (Version 14 CEROS, Hamilton Thorne Research) with a Slide Warmer (#720230, Hamilton Thorne Research). The following parameters were used: acquisition of 30 frames at a frame rate of 60 Hz, Minimum Contrast: 30, Minimum Cell Size: 4 Pixels, Minimum Static Contrast: 15.

Sperm Head–Tail Separation.

Collect the mouse sperm use liquid nitrogen freezing-thawed for several times. Subsequently, the sample was centrifuged at 10,000× g for 5 minutes, and the pellet was resuspended in 200 μL of PBS. The resuspended sample was mixed with 1.8 mL of 90% Percoll solution (sigma, P1644) and then subjected to centrifugation at 15,000 × g for 15 minutes. Following centrifugation, the sperm head accumulated at the bottom while the sperm tail remained at the top of the tube. Sperm head and tail were mixed with PBS 5 times their volume, and centrifuged at 10000 × g for 5 min. Subsequently, the sperm head and tail were washed twice with PBS, followed by lysing using a lysate buffer (PH=7.6, 50mM Tris-HCl, 150mM NaCl, 1%TritonX-100, 0.5% sodium deoxycholate, 0.1% SDS, 2mM EDTA), protease inhibitor cocktail (Roche, 04693116001) was added to the lysate proportionally. Add 1/5 volume of 5× loading (PH=6.8,10% SDS, 25% Glycerol, 1M Tris-HCL, 5% β-mercaptoethanol, and 0.25% bromophenol blue dye). The mixture was boiled at 100 °C for 10 minutes, and the supernatant was collected as the sample after centrifugation.

Separation of different fraction of Sperm.

The separation process for different fractions of sperm was performed as previously described (34, 35, 59). Briefly, the sperm collected from the cauda were washed twice with PBS and resuspended in 1% Triton X-100 lysis buffer (50 mM NaCl, 20 mM Tris·HCl, pH 7.5, protease inhibitor mixture) with a protease inhibitor mixture. The samples were then incubated at 4 °C for 2 hours and subsequently centrifuged at 15,000× g for 10 minutes. The resulting supernatant was collected as the Triton-soluble fraction. The pellet was resuspended in 1% SDS lysis buffer (75 mM NaCl, 24 mM EDTA, pH 6.0) and incubated at room temperature for 1 hour. After centrifugation, the supernatant was collected as the SDS-soluble fraction. The residual pellet was boiled in sample buffer (66 mM TRIS-HCL, 2% SDS, 10% glycerol and 0.005% Bromophenol Blue) for 10min. The supernatant obtained after centrifugation was collected as the SDS-resistant fraction. Before use, a protease inhibitor cocktail (Roche, 04693116001) was added to the 1% Triton X-100 lysis buffer and the 1% SDS lysis buffer in the appropriate proportion.

Transmission electronic microscopy.

Transmission electron microscopy (TEM) was performed at the Centre for Electron Microscopy of the National Institute of Biological Sciences, Beijing, following standard protocols. Briefly, the epididymis cauda was taken and fixed overnight at 4℃ using a 2.5% glutaraldehyde fixing solution (Sigma-Aldrich, G5882). After washing three times with PBS for 20 minutes each time, the samples were fixed at room temperature for 1 hour using 1% Osmium tetroxide. Subsequently, the samples were washed three times with PBS for 20 minutes each time. The samples were then dehydrated using a series of ascending acetone solutions by the progressive lowering temperature method, followed by epoxy and resin embedding. The embedded blocks were placed in a drying oven at 45℃ for 12 hours and then at 60℃ for three days. Ultra-thin slices were obtained and stained with 3% uranyl acetate in 70% methanol/H2O, followed by Sato's lead for 2 minutes. Images were captured using a TECNAI spirit G2 (FEI) transmission electron microscope at 120 Kv.

Western blot.

Samples from various mouse tissues were collected and digested with lysate (PH=7.6, 50mM Tris-HCl, 150mM NaCl, 1%TritonX-100, 0.5% sodium deoxycholate, 0.1% SDS, 2mM EDTA). protease inhibitor cocktail (Roche, 04693116001) was added into the lysate proportionally before use. The lysate was then mixed with 1/5 volume of 5× loading buffer (10% SDS, 25% glycerol, 1M Tris-HCl, 5% β-mercaptoethanol, and 0.25% bromophenol blue dye, pH 6.8). The mixture was boiled at 100 °C for 10 minutes, followed by centrifugation to obtain the supernatant as the sample. Proteins were separated by SDS/PAGE and transferred to PVDF membranes. The membranes were blocked with 5% skim milk in TBST (pH 7.6, 20 mM Tris, 150 mM NaCl with 0.05% Tween-20) for 1 hour. Incubation with primary antibody overnight at 4 °C. Washing the membrane three times with TBST for 10 minutes each time, the membranes were incubated with the secondary antibody at room temperature for 1 hour. Subsequently, the membranes were washed three times with TBST. ECL reagents (BIO-RAD, 170-5060 or NCM Biotech, P10300B) were added onto membranes, and signals were detected by XBT X-ray film (Carestream, 6535876).

Immunofluorescence.

Collect mouse sperm in preheated PBS at 37 °C for 15 minutes. Discard the cauda tissue and centrifuge the remaining solution at 1000x g for 5 minutes. The epididymis tissue was discarded, centrifuged at 1000× g for 5min, fixed at room temperature with 4% paraformaldehyde (DF0135; Beijing Leagene Biotech) for 30min, spread on the slide, and dried at room temperature. Antigen repair was performed with antigen repair solution (10 mM sodium citrate, 0.05% Tween-20, pH 6.0), cooled to room temperature, and then blocked with ADB (3% BSA, 0.05% TritonX-100) at room temperature for 1 hour. The primary antibody (anti-FLAG M2) was incubated overnight and washed with PBST (PBS with 0.1% Tween-20) three times for 5min each time. The secondary antibodies (Alexa Fluor® 546-conjugated donkey anti-mouse IgG and Alexa Fluor® 647-conjugated donkey anti-rabbit IgG) and Hoechst 33342 (Sigma, #b2261) were incubated with the samples at room temperature for 1 hour away from light. After incubation, the samples were washed three times with PBST (PBS with 0.1% Triton X-100) for 5 minutes each. Confocal microscopy was performed using a Nikon SIM microscope to acquire images.

Identification of interacting proteome by LC-MS

Protein bands were carefully excised from the polyacrylamide gel using a razor blade, minimizing the inclusion of excess blank gel. The excised gel bands were further trimmed into smaller pieces and transferred into 1.5 mL microcentrifuge tubes for processing. The gel pieces were destained three times using 25 mM ammonium bicarbonate (NH_4HCO_3) in 50% methanol, with each destaining step lasting 10 minutes. Subsequently, the gel fragments were washed three times with a solution of 10% acetic acid in 50% methanol, with each wash lasting 1 hour. Afterward, the gel pieces were rinsed twice with water for 20 minutes each time to ensure removal of residual reagents. The gel pieces were then transferred into 0.5 mL microcentrifuge tubes. To dehydrate the gel fragments, 0.5 mL of 100% acetonitrile (ACN) was added, and the tubes were gently inverted several times until the gel pieces turned opaque white. The ACN was subsequently

removed, and the gel pieces were dried using a SpeedVac system for 20–30 minutes under mild heating conditions. For protein digestion, the gel pieces were rehydrated with 5–20 μL of trypsin solution (10 ng/Ml) in 50 mM NH_4HCO_3, pH 8.0). The samples were then incubated at 37 °C overnight to allow for proteolysis. Following digestion, the gel pieces were soaked in 25–50 μL of 50% ACN with 5% formic acid (FA) for 30–60 minutes with gentle agitation, taking care not to vortex the samples. The resulting supernatant was transferred to a fresh 0.5 mL microcentrifuge tube. The gel pieces were then subjected to a second extraction using 25–50 μL of 75% ACN with 0.1% FA, again with gentle agitation for 30–60 minutes. The supernatants from both extractions were combined and dried completely using the SpeedVac system under slight heating conditions, ensuring that the peptides were fully recovered for further analysis.

Protein interactions were verified in 293T cells by co-immunoprecipitation

The protein-coding gene was obtained through the NCBI database and subsequently cloned into the pcDNA3.1 vector. The primers used for vector construction are provided in the supplementary materials (Supplementary Material 1). The plasmid was transfected into 293T cells using the jetOPTIMUS® transfection reagent (catalog number: 101000006), and the cells were cultured at 37 °C with 5% CO_2 for 36 hours. After incubation, the culture medium was discarded, and the cells were gently washed once with PBS to remove any residual medium. Cell lysis was performed using RIPA lysis buffer (pH 7.6: 50 mM Tris-HCl, 150 mM NaCl, 1% Triton X-100 or 1% NP-40, 2 mM EDTA). A portion of the lysate was reserved as the input control, while the remaining lysate was divided into two equal parts. One part was used for FLAG immunoprecipitation (IP) and the other for MYC IP. Both were incubated overnight at 4 °C to allow sufficient binding. The beads were washed with RIPA lysis buffer a total of five times, with each wash lasting 3 minutes. To elute the bound proteins, 1X SDS loading buffer was added to the beads, and the samples were denatured by heating at 95 °C for 5 minutes.

Proteomic analysis of whole sperm

The samples were pulverized into a fine powder using liquid nitrogen and then transferred to a tube. A lysis buffer (8 M urea, 1% protease inhibitor cocktail) was added at a 1:4 ratio, and the mixture was sonicated for 3 minutes on ice using a Scientz high-intensity ultrasonic processor. The lysate was centrifuged at 12,000 g for 10 minutes at 4 °C, and the supernatant was collected. Protein concentration was measured using a BCA assay kit. For digestion, proteins were treated with 5 mM DTT at 56 °C for 30 minutes to reduce disulfide bonds, then alkylated with 11 mM iodoacetamide for 15 minutes in the dark. The sample was diluted with 200 mM TEAB to lower the urea concentration to under 2 M. Trypsin was added at ratio of 1:50 for an overnight digestion, followed by a second digestion at a 1:100 ratio for 4 hours. Peptides were purified using a Strata X SPE column. For mass spectrometry analysis, peptides were dissolved in solvent A (0.1% formic acid, 2% acetonitrile in water) and separated on a 25 cm home-made reversed-phase column with a 100 μm diameter. A gradient elution from 6% to 80% solvent B (0.1% formic acid, 90% acetonitrile) over 20 minutes was used at a flow rate of 700 nL/min with an EASY-nLC 1200 UPLC system. Peptide separation was followed by analysis on an Orbitrap Exploris 480 mass spectrometer, with full MS scans at a 60,000 resolution and MS/MS scans at 15,000 resolution using HCD at 27% NCE. DIA data were processed using the DIA-NN software. Spectra were searched against the Mus_musculus_10090_SP_20231220.fasta database, with Trypsin/P specified as the enzyme and up to one missed cleavage allowed. Fixed modifications included N-terminal methionine removal and carbamidomethylation of cysteine residues. The false discovery rate (FDR) was controlled below 1%.

Measurement of Sperm ATP level.

Collect mouse sperm in preheated PBS at 37 °C for 15 minutes. The cauda tissue was discarded, and the remaining solution was centrifuged at 1000× g for 5 minutes. The pellets were then washed twice with PBS. After sperm count, 1×10^7 sperm per well were added to 96-well plates, followed by adding 30μL of lysate (Promega, G7570). The level of ATP was measured using a

MicroPlate Spectrophotometer (TECAN) after shaking the plates on a shaker for 20 minutes away from light.

Evaluation of mitochondrial activity of spermatozoa using TMRM.

Sperm were collected from the epididymis cauda and mitochondrial membrane potential was detected by TMRM (Invitrogen, I34361) (60). Briefly, collect mouse sperm in preheated PBS at 37 °C for 15 minutes. Discard the cauda tissue and centrifuge the remaining solution at 300x g for 5 minutes. Wash the pellets twice with DPBS. Incubate the washed sperm with TMRM for 30 minutes at 37℃ and 5% CO2. After incubation, wash the sperm twice with DPBS to remove any unbound dye. Resuspend the pellet and mix it with DAPI, then spread on the slide. Capture fluorescence images using the DAPI filter (405nm) and RFP filter (560nm).

Evaluation of ROS level.

Spermatozoa were obtained from the cauda epididymis and incubated for 50 minutes in preheated TYH medium (manufacturer, catalog number) with or without Rosup. Subsequently, the samples underwent a gentle centrifugation at 300Xg for 4 minutes, followed by resuspension in 1 mL of DCFDA mix. The DCFDA mix was prepared by diluting DCFH-DA (Beyotime, S0033S) in a 1:1000 ratio with TYH medium. After an incubation at 37 °C with 5% CO2 for 20 minutes, inversion mixing was performed every 5 minutes to ensure proper distribution. The samples were then subjected to another centrifugation step at 300Xg for 4 minutes to remove the supernatant. Pellets were washed three times with DPBS to eliminate any residual DCFH-DA that had not penetrated the intracellular compartments. Following this, the pellets were resuspended, mixed with DAPI, and subsequently spread onto slides. Fluorescence images were captured using a DAPI filter (405nm) and an FITC filter (510-580nm).

Sample preparation of mouse sperm axoneme.

Freshly extracted sperm were centrifuged at 400 G (Thermo Scientific Legend Micro 17 R) for 5 min at 4 °C. The precipitate per 100μL semen was carefully re-suspended in 100μL of precooled PBS and diluted 5.5-fold with PBS before use. The cryo-EM carrier network (Quantifoil R3.5/1, Au 200 mesh) was discharged for 60 s using Gatan Solarus. Sperm samples were quickly frozen by vitrification using Leica EMGP. Samples diluted in 3μL PBS were immediately water absorbed at 100% relative humidity and 4 °C for 3-5s, and then the frozen samples were placed in a mixture of ethane and methane cooled to -195 °C and stored in liquid nitrogen for cryo-FIB thinning. The cryo-FIB thinning strategy was referred to in the previous work (46).

Cryo-ET tilt series acquisition.

The grid after the reduction of cryo-FIB was mounted onto Autoloader in Titan Krios G3 (Thermofisher Scientific) 300 KV TEM, equipped with a Gatan K2 direct electron detector (DED) and a BioQuantum energy filter. Tilt series were collected at a magnification of ×42,000, resulting in a physical pixel size of 3.4 Å in K2 DED and 3.4 Å in counting mode. Before data collection, the pre-tilt of the sample was determined visually, and the pre-tilt was set to 10° or -9° to match the pre-determined geometry induced by loading grids. The total dose for each tilt was set to 3.5 electrons per angstrom squared, divided into 10 frames over a 1.2-s exposure, and the tilt range was set to -9° pre-tilt of -66° to +51°, or +10° pre-tilt of -50° to +67°, in steps of 3°, resulting in 40 tilts and 140 electrons per tilt series. The slit width was set to 20 eV, zero loss peaks were refined after the collection of each tilt series, and nominal defocus was set from -1.8 to -2.5 μm. All tilt series used in this study were collected using a beam-image-shift facilitated acquisition scheme based on a dose symmetry strategy using a script developed in-house in SerialEM software (61-63).

Mouse sperm axoneme *in situ* data processing.

After data collection, all fractioned movies were imported into Warp for essential processing, including motion correction, 2-x Fourier segmentation of super-resolution frames, CTF estimation, masking platinum islands or other high-contrast features, and tilt series generation. Subsequently, the tilt series was automatically aligned using AreTOMO (45, 64). Aligned tilt series were visually inspected in IMOD and any low-quality frames (such as those blocked by the sample stage or grid bars, containing obvious crystalline ice or showing obvious jumps) were removed to create new sets of tilt series in Warp. The new tilt series underwent a second round of AreTOMO alignment. Then, low-quality frames were removed again using the same criteria as in the first round. The new tilt series was then subjected to a third round of automatic alignment, continuing the process until there were no frames to remove. After tilt series alignment, those tilt series that were less than 30 frames or failed were not further processed (43, 45). The alignment parameters of all remaining tilt series were passed back to Warp, and initial tomogram reconstruction was performed in Warp at 27.2 Å pixel size, resulting in a total of 160 Bin8 tomograms (44).

Among the total 160 tomograms, we used the filament picking tool in Dynamo to manually pick DMT particles from 89 of all tomograms. By selecting the starting and ending points of each DMT fiber, and separating each cutting point by 8 nm along the fiber axis, we were able to obtain 89 sets of DMT particles (65). The 3D coordinates and two of the three Euler angles (except for in-plane rotation) are automatically generated by Dynamo and then transferred back to Warp for exporting sub-tomograms (44, 65, 66).

In RELION 3.1, sub-tomograms were refined, using the ABTT package to transform the RELION star file and Dynamo table file and use Dynamo and/or RELION to jointly generate a mask (47, 49). First, all particles were reconstructed into the box size of 48^3 voxels with a pixel size of 27.2 Å, and all extracted particles were directly averaged and low-pass filtered at 80 Å to generate an initial reference. Then 3D classification with K = 1 was performed under the constraints of the first two Euler angles (—sigma_tilt 3 and —sigma_psi 3 in RELION), and 3D automatic refinement was performed after 25 iterations. After alignment, manually cleaned the particles in Chimerax-1.6 (46, 67), and then transferred these aligned parameters back to Warp to export the sub-tomograms with a box size of 84^3 voxels and a pixel size of 13.6 Å. The particles were automatically refined in RELION. After removing any duplicate particles in Dynamo, we transferred these aligned parameters back to Warp to export the sub-tomograms with the box size of 128^3 voxels and the pixel size of 6.8 Å. Then it was automatically refined in RELION and M with a final resolution of 24 Å (47-49).

GSEA analysis

The protein mass spectrometry utilized three controls and three ANKRD5 KO mice. Dropout data were imputed using KNN, followed by log2 normalization and sorting to obtain the final data list. Mouse gene symbols were converted to Entrez IDs using the org.Mm.eg.db annotation package, and GSEA analysis was performed with the clusterProfiler package (68). The term 'Glycolysis and Gluconeogenesis' is obtained from KEGG. Mouse gene sets were retrieved from the MSigDB (Molecular Signature Database) via the msigdbr package, focusing on category C2, which includes various biological processes and pathways. The analysis was conducted in R version 4.4.1 (2024-06-14 ucrt).

Statistical analysis.

All data are presented as the mean ± SEM (n≥3). Statistical analysis was performed using Student's t-test or one-way ANOVA. GraphPad Prism version 9.4.1 was used for the analysis, and results were considered significant when $P < 0.05$. Adobe Illustrator 2021 was used for image layout.

Acknowledgments

We thank the Transgenic Animal Center at the National Institute of Biological Sciences, Beijing, for their support in generating and maintaining the transgenic mice. We are also grateful to Professor Fei Sun's group at the Institute of Biophysics, Chinese Academy of Sciences, for their

technical assistance in Cryo-ET. Additionally, we appreciate the staff at the Electron Microscopy Center and the Imaging Center of the National Institute of Biological Sciences, Beijing, for their technical support in imaging. We also extend our thanks to the State Key Laboratory for Animal Biotechnology at the College of Biological Sciences, China Agricultural University, for their help in the analysis of mouse sperm motility. This work was supported by the Beijing Natural Science Foundation (JQ24056 to Y.Z.) and the National Natural Science Foundation of China (32471244 to Y.Z.).

References

1. H. H. Bhakta, F. H. Refai, M. A. Avella, The molecular mechanisms mediating mammalian fertilization. *Development* **146** (2019).
2. A. Agarwal, et al., Male infertility. *Lancet* **397**, 319-333 (2021).
3. A. Barrell, Data from "How does sperm motility affect fertility?". Available at https://www.medicalnewstoday.com/articles/320160. Deposited 2024-10-13 15:48:00.
4. S. Lu, et al., Probing meiotic recombination and aneuploidy of single sperm cells by whole-genome sequencing. *Science* **338**, 1627-1630 (2012).
5. S. Dey, C. Brothag, S. Vijayaraghavan, Signaling enzymes required for sperm maturation and fertilization in mammals. *Front. Cell. Dev. Biol.* **7**, 341 (2019).
6. Z. Heidary, K. Saliminejad, M. Zaki-Dizaji, K. H. Khorram, Genetic aspects of idiopathic asthenozoospermia as a cause of male infertility. *Hum. Fertil.* **23**, 83-92 (2020).
7. D. M. Campagne, Should fertilization treatment start with reducing stress? *Hum. Reprod.* **21**, 1651-1658 (2006).
8. H. Miyata, A. Morohoshi, M. Ikawa, Analysis of the sperm flagellar axoneme using gene-modified mice. *Exp. Anim.* **69**, 374-381 (2020).
9. K. Inaba, Molecular architecture of the sperm flagella: molecules for motility and signaling. *Zool. Sci.* **20**, 1043-1056 (2003).
10. K. Yogo, Molecular basis of the morphogenesis of sperm head and tail in mice. *Reprod. Med. Biol.* **21**, e12466 (2022).
11. J. Awata, et al., Drc3 connects the n-drc to dynein g to regulate flagellar waveform. *Mol. Biol. Cell* **26**, 2788-2800 (2015).
12. R. Bower, et al., Drc2/ccdc65 is a central hub for assembly of the nexin-dynein regulatory complex and other regulators of ciliary and flagellar motility. *Mol. Biol. Cell* **29**, 137-153 (2018).
13. R. Bower, et al., The n-drc forms a conserved biochemical complex that maintains outer doublet alignment and limits microtubule sliding in motile axonemes. *Mol. Biol. Cell* **24**, 1134-1152 (2013).
14. T. Heuser, M. Raytchev, J. Krell, M. E. Porter, D. Nicastro, The dynein regulatory complex is the nexin link and a major regulatory node in cilia and flagella. *J. Cell Biol.* **187**, 921-933 (2009).
15. L. C. Gardner, E. O'Toole, C. A. Perrone, T. Giddings, M. E. Porter, Components of a "dynein regulatory complex" are located at the junction between the radial spokes and the dynein arms in chlamydomonas flagella. *J. Cell Biol.* **127**, 1311-1325 (1994).
16. T. Oda, H. Yanagisawa, M. Kikkawa, Detailed structural and biochemical characterization of the nexin-dynein regulatory complex. *Mol. Biol. Cell* **26**, 294-304 (2015).
17. T. Oda, T. Yagi, H. Yanagisawa, M. Kikkawa, Identification of the outer-inner dynein linker as a hub controller for axonemal dynein activities. *Curr. Biol.* **23**, 656-664 (2013).
18. J. Lin, et al., Building blocks of the nexin-dynein regulatory complex in chlamydomonas flagella. *J. Biol. Chem.* **286**, 29175-29191 (2011).
19. A. Ghanaeian, et al., Integrated modeling of the nexin-dynein regulatory complex reveals its regulatory mechanism. *Nat. Commun.* **14**, 5741 (2023).
20. L. Gui, et al., Scaffold subunits support associated subunit assembly in the chlamydomonas ciliary nexin-dynein regulatory complex. *Proc. Natl. Acad. Sci. U. S. A.* **116**, 23152-23162 (2019).
21. C. Austin-Tse, et al., Zebrafish ciliopathy screen plus human mutational analysis identifies c21orf59 and ccdc65 defects as causing primary ciliary dyskinesia. *Am. J. Hum. Genet.* **93**,

672-686 (2013).
22. B. Huang, Z. Ramanis, D. J. Luck, Suppressor mutations in chlamydomonas reveal a regulatory mechanism for flagellar function. *Cell* **28**, 115-124 (1982).
23. M. Wirschell, et al., The nexin-dynein regulatory complex subunit drc1 is essential for motile cilia function in algae and humans. *Nature Genet.* **45**, 262-268 (2013).
24. P. Satir, Studies on cilia. 3. Further studies on the cilium tip and a "sliding filament" model of ciliary motility. *J. Cell Biol.* **39**, 77-94 (1968).
25. K. E. Summers, I. R. Gibbons, Adenosine triphosphate-induced sliding of tubules in trypsin-treated flagella of sea-urchin sperm. *Proc. Natl. Acad. Sci. U. S. A.* **68**, 3092-3096 (1971).
26. D. M. Woolley, Studies on the eel sperm flagellum. I. The structure of the inner dynein arm complex. *J. Cell Sci.* **110 (Pt 1)**, 85-94 (1997).
27. J. Zhang, et al., Loss of drc1 function leads to multiple morphological abnormalities of the sperm flagella and male infertility in human and mouse. *Hum. Mol. Genet.* **30**, 1996-2011 (2021).
28. S. Ha, A. M. Lindsay, A. E. Timms, D. R. Beier, Mutations in dnaaf1 and lrrc48 cause hydrocephalus, laterality defects, and sinusitis in mice. *G3-Genes Genomes Genet.* **6**, 2479-2487 (2016).
29. J. M. Castaneda, et al., Tcte1 is a conserved component of the dynein regulatory complex and is required for motility and metabolism in mouse spermatozoa. *Proc. Natl. Acad. Sci. U. S. A.* **114**, E5370-E5378 (2017).
30. A. Morohoshi, et al., Nexin-dynein regulatory complex component drc7 but not fbxl13 is required for sperm flagellum formation and male fertility in mice. *Plos Genet.* **16**, e1008585 (2020).
31. R. K. Li, et al., Iqcg is essential for sperm flagellum formation in mice. *Plos One* **9**, e98053 (2014).
32. H. Gan, et al., Dynamics of 5-hydroxymethylcytosine during mouse spermatogenesis. *Nat. Commun.* **4**, 1995 (2013).
33. E. Kim, et al., Sperm penetration through cumulus mass and zona pellucida. *Int. J. Dev. Biol.* **52**, 677-682 (2008).
34. W. Cao, G. L. Gerton, S. B. Moss, Proteomic profiling of accessory structures from the mouse sperm flagellum. *Mol. Cell. Proteomics* **5**, 801-810 (2006).
35. H. Miyata, et al., Spata33 localizes calcineurin to the mitochondria and regulates sperm motility in mice. *Proc. Natl. Acad. Sci. U. S. A.* **118** (2021).
36. A. Lewit-Bentley, S. Rety, Ef-hand calcium-binding proteins. *Curr. Opin. Struct. Biol.* **10**, 637-643 (2000).
37. A. J. Koppers, G. N. De Iuliis, J. M. Finnie, E. A. McLaughlin, R. J. Aitken, Significance of mitochondrial reactive oxygen species in the generation of oxidative stress in spermatozoa. *The Journal of Clinical Endocrinology & Metabolism* **93**, 3199-3207 (2008).
38. S. Kothari, A. Thompson, A. Agarwal, S. S. du Plessis, Free radicals: their beneficial and detrimental effects on sperm function (2010).
39. A. Amaral, B. Lourenço, M. Marques, J. Ramalho-Santos, Mitochondria functionality and sperm quality. *Reproduction* **146**, R163-R174 (2013).
40. J. Baumber, B. A. Ball, J. J. Linfor, S. A. Meyers, Reactive oxygen species and cryopreservation promote dna fragmentation in equine spermatozoa. *Journal of Andrology* **24**, 621-628 (2003).
41. Z. Gibb, S. R. Lambourne, R. J. Aitken, The paradoxical relationship between stallion fertility and oxidative stress. *Biol. Reprod.* **91**, 77, 1-10 (2014).
42. F. Barbagallo, et al., Evaluation of sperm mitochondrial function: a key organelle for sperm motility. *J. Clin. Med.* **9**, 363 (2020).
43. J. R. Kremer, D. N. Mastronarde, J. R. McIntosh, Computer visualization of three-dimensional image data using imod. *J. Struct. Biol.* **116**, 71-76 (1996).
44. D. Tegunov, P. Cramer, Real-time cryo-electron microscopy data preprocessing with warp. *Nat. Methods* **16**, 1146-1152 (2019).
45. S. Zheng, et al., Aretomo: an integrated software package for automated marker-free, motion-corrected cryo-electron tomographic alignment and reconstruction. *J. Struct. Biol.- X* **6**, 100068 (2022).
46. L. Tai, G. Yin, X. Huang, F. Sun, Y. Zhu, In-cell structural insight into the stability of sperm microtubule doublet. *Cell Discov.* **9**, 116 (2023).
47. S. H. Scheres, Relion: implementation of a bayesian approach to cryo-em structure

determination. *J. Struct. Biol.* **180**, 519-530 (2012).
48. D. Tegunov, L. Xue, C. Dienemann, P. Cramer, J. Mahamid, Multi-particle cryo-em refinement with m visualizes ribosome-antibiotic complex at 3.5 a in cells. *Nat. Methods* **18**, 186-193 (2021).
49. J. Zivanov, et al., New tools for automated high-resolution cryo-em structure determination in relion-3. *Elife* **7** (2018).
50. T. Walton, et al., Axonemal structures reveal mechanoregulatory and disease mechanisms. *Nature* **618**, 625-633 (2023).
51. S. S. Suarez, A. A. Pacey, Sperm transport in the female reproductive tract. *Hum. Reprod. Update* **12**, 23-37 (2006).
52. S. S. Suarez, X. Dai, Hyperactivation enhances mouse sperm capacity for penetrating viscoelastic media. *Biol. Reprod.* **46**, 686-691 (1992).
53. Y. Fujihara, H. Miyata, M. Ikawa, Factors controlling sperm migration through the oviduct revealed by gene-modified mouse models. *Exp. Anim.* **67**, 91-104 (2018).
54. T. Wakayama, et al., Penetration by field vole spermatozoa of mouse and hamster zonae pellucidae without acrosome reaction. *J Reprod Fertil* **107**, 97-102 (1996).
55. J. Li, A. Mahajan, M. D. Tsai, Ankyrin repeat: a unique motif mediating protein-protein interactions. *Biochemistry* **45**, 15168-15178 (2006).
56. H. A. Chung, T. S. Yamamoto, N. Ueno, Anr5, an fgf target gene product, regulates gastrulation in xenopus. *Curr. Biol.* **17**, 932-939 (2007).
57. C. Zou, et al., Bioinformatics analysis identifies potential hub genes and crucial pathways in the pathogenesis of asthenozoospermia. *Bmc Med. Genomics* **15**, 252 (2022).
58. L. Jeanson, et al., Mutations in gas8, a gene encoding a nexin-dynein regulatory complex subunit, cause primary ciliary dyskinesia with axonemal disorganization. *Hum. Mutat.* **37**, 776-785 (2016).
59. H. Miyata, et al., Testis-enriched kinesin kif9 is important for progressive motility in mouse spermatozoa. *Faseb J.* **34**, 5389-5400 (2020).
60. J. Dalal, A. Kumar, M. Honparkhe, D. Deka, N. Singh, Minimization of apoptosis-like changes in cryopreserved buffalo bull sperm by supplementing extender with bcl-2 protein. *Vet. World* **9**, 432-436 (2016).
61. W. Hagen, W. Wan, J. Briggs, Implementation of a cryo-electron tomography tilt-scheme optimized for high resolution subtomogram averaging. *J. Struct. Biol.* **197**, 191-198 (2017).
62. D. N. Mastronarde, Automated electron microscope tomography using robust prediction of specimen movements. *J. Struct. Biol.* **152**, 36-51 (2005).
63. C. Wu, X. Huang, J. Cheng, D. Zhu, X. Zhang, High-quality, high-throughput cryo-electron microscopy data collection via beam tilt and astigmatism-free beam-image shift. *J. Struct. Biol.* **208**, 107396 (2019).
64. D. Tegunov, P. Cramer, 1-real-time cryo-electron microscopy data preprocessing with warp. *Nat. Methods* **16**, 1146-1152 (2019).
65. D. Castano-Diez, M. Kudryashev, M. Arheit, H. Stahlberg, Dynamo: a flexible, user-friendly development tool for subtomogram averaging of cryo-em data in high-performance computing environments. *J. Struct. Biol.* **178**, 139-151 (2012).
66. A. Burt, L. Gaifas, T. Dendooven, I. Gutsche, A flexible framework for multi-particle refinement in cryo-electron tomography. *Plos. Biol.* **19**, e3001319 (2021).
67. T. D. Goddard, et al., Ucsf chimerax: meeting modern challenges in visualization and analysis. *Protein Sci.* **27**, 14-25 (2018).
68. T. Wu, et al., Clusterprofiler 4.0: a universal enrichment tool for interpreting omics data. *Innovation (Camb)* **2**, 100141 (2021).

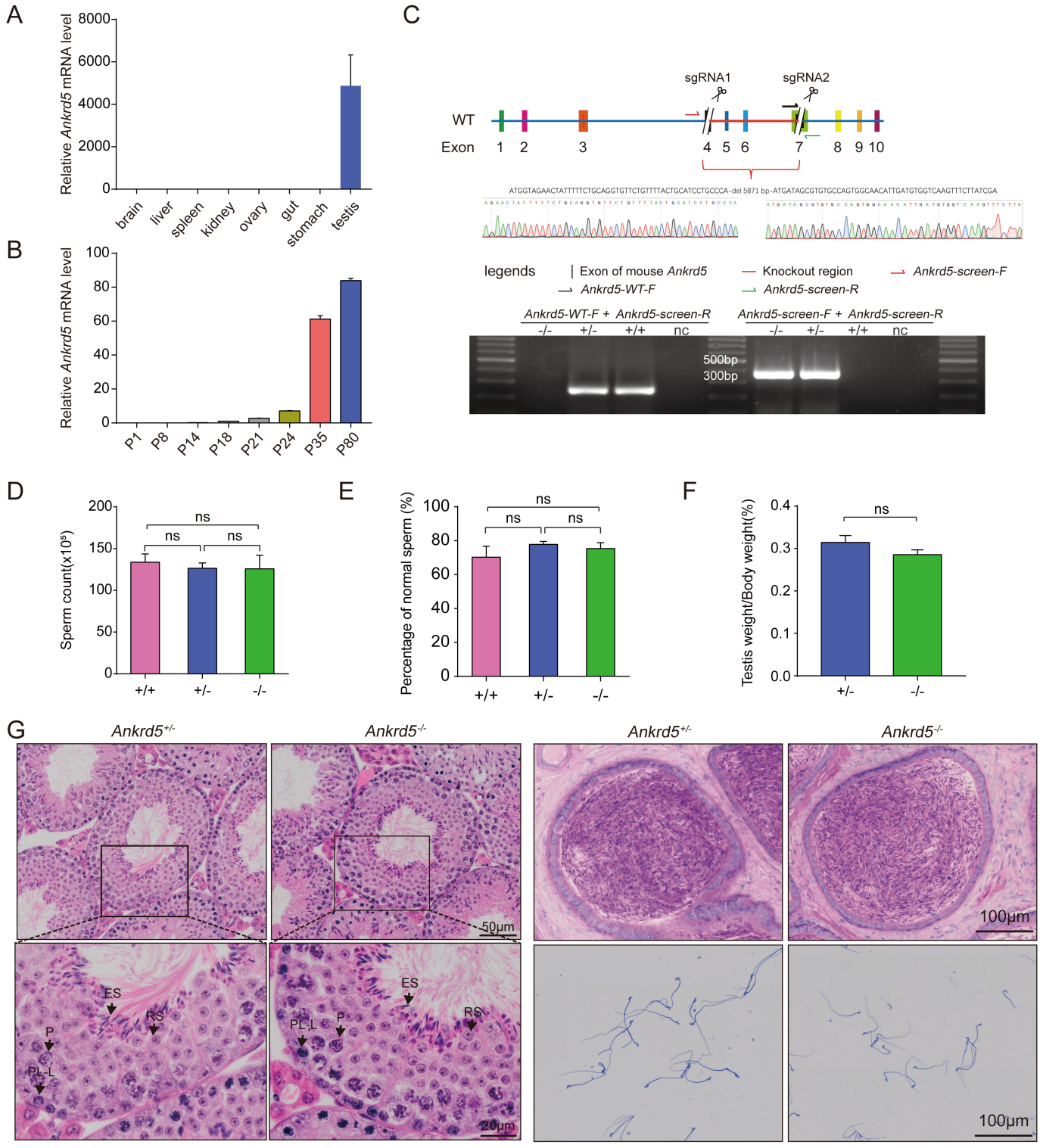

Figure 1. *Ankrd5* is critical for male reproductive function. (A and B) Relative expression of *Ankrd5* mRNA in different tissues of adult mouse and testes at various postnatal days. The *Ankrd5* mRNA expression levels were normalized to the expression of *Gapdh* mRNA (n=3). (C) CRISPR/Cas9 targeting scheme of mouse *Ankrd5* and genotyping of *Ankrd5* KO mouse. *Ankrd5- WT- F* + *Ankrd5-screen- R* (for WT) and *Ankrd5-screen-F* + *Ankrd5-screen-R* (for KO). nc, negative control (ddH2O). (D and E) Sperm count and percentage of normal sperm of cauda epididymal from control and *Ankrd5* KO mouse (n=5). (F) Testis to body weight ratio of adult control and *Ankrd5* KO mouse (n=7). (G) Hematoxylin and eosin (H&E) staining of mouse testis and epididymis. Coomassie Brilliant Blue R-250 staining of spermatozoa from control and *Ankrd5* KO male mouse. No significant abnormality was found in *Ankrd5* KO male mouse. No overt abnormalities were found in *Ankrd5* KO mouse. P, pachytene; ES, elongated sperm; RS, round sperm; SG, spermatogonia; ST, Sertoli cell. All values in this figure are shown as the mean ± SE.

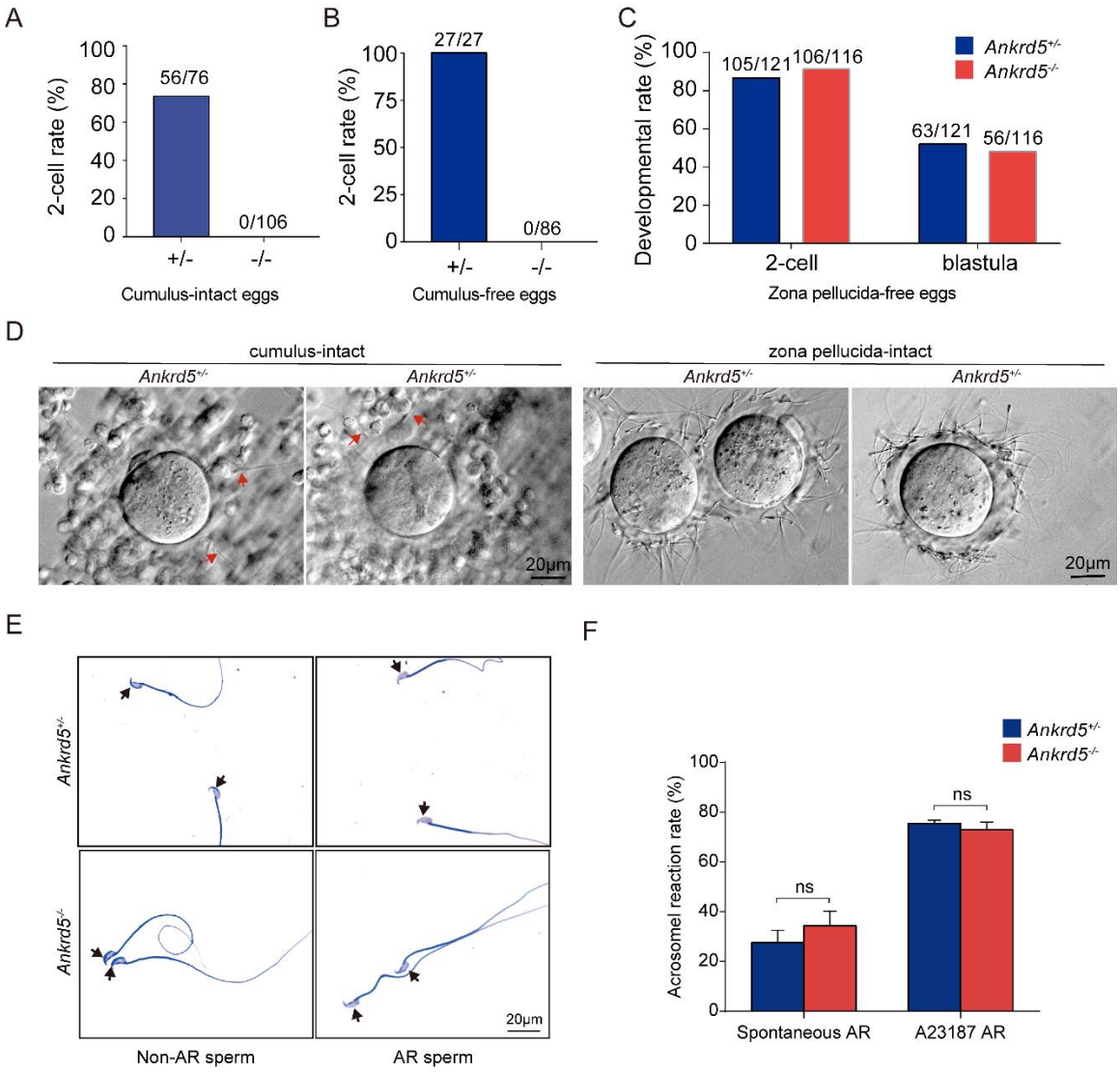

Figure 2. Evaluation of in vitro fertilization capacity of *Ankrd5* KO sperm. (A-C) Fertilization rate of IVF using control and *Ankrd5* KO spermatozoa. Three types of oocytes (cumulus-intact, cumulus-free, and zona pellucida-free) were used for IVF. (D) Egg observation after IVF. After 4 hours of incubation, both of control and *Ankrd5* KO sperm could penetrate cumulus oophorus as indicated by the red arrow and have the ability to bind to the zona pellucida. (E and F) Sperm were incubated in capacitation medium treated with A23187 (dissolved in DMSO) and DMSO (dissolvent control group) and stained with Coomassie Brilliant Blue R-250. Black arrow indicates the intact or disappeared acrosome; Values represent mean ± SE (n=3).

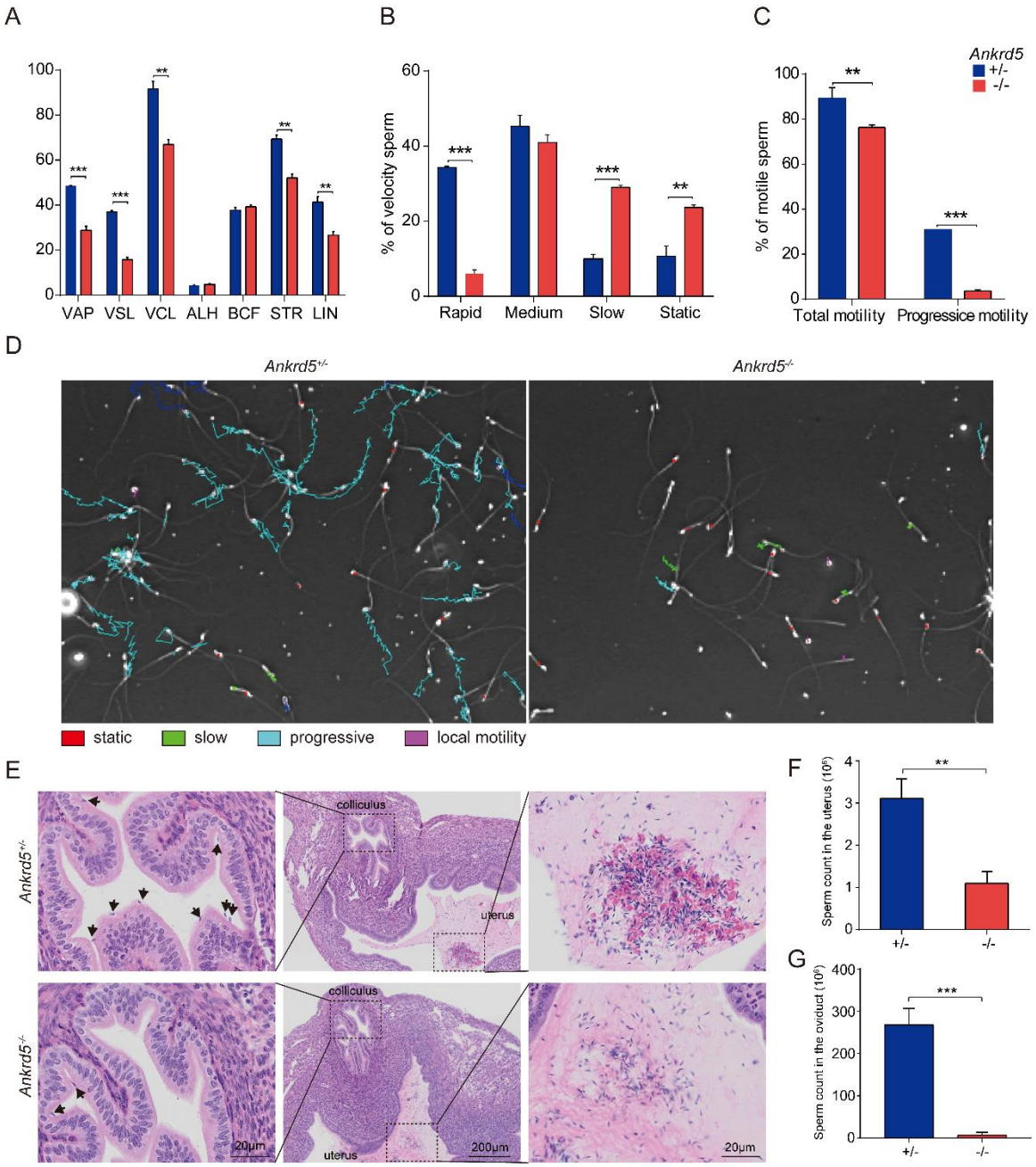

Figure 3. Sperm motility of *Ankrd5* KO male mouse. (A) Average path velocity (VAP), straight line velocity (VSL), curvilinear velocity (VCL), amplitude of lateral head displacement (ALH), beat cross frequency (BCF), straightness (STR), and linearity (LIN) of sperm from control and *Ankrd5* KO mouse. **P < 0.01, ***P < 0.001, Student's t test; error bars represent SE (n = 3). (B) Proportions of sperm at different velocity levels in control and *Ankrd5* KO mouse. **P < 0.01, ***P < 0.001, Student's t test; error bars represent SE (n = 3). (C) Knockout mouse had lower motile sperm (total motor capacity) and progressive motile sperm (progressive motor capacity) than control. **P < 0.01, ***P < 0.001, Student's t test; error bars represent SE (n = 3). (D) Trajectories of sperm per second. The meanings of different colors are shown in the graph. (E) Impaired migration of *Ankrd5* KO sperm from uterus into oviducts. The black arrow indicates sperm. (F and G) Numbers of sperm from control and *Ankrd5* KO mouse in female uterus and oviducts after mating. **P < 0.01, ***P <0.001, Student's t test; error bars represent SE (n = 3).

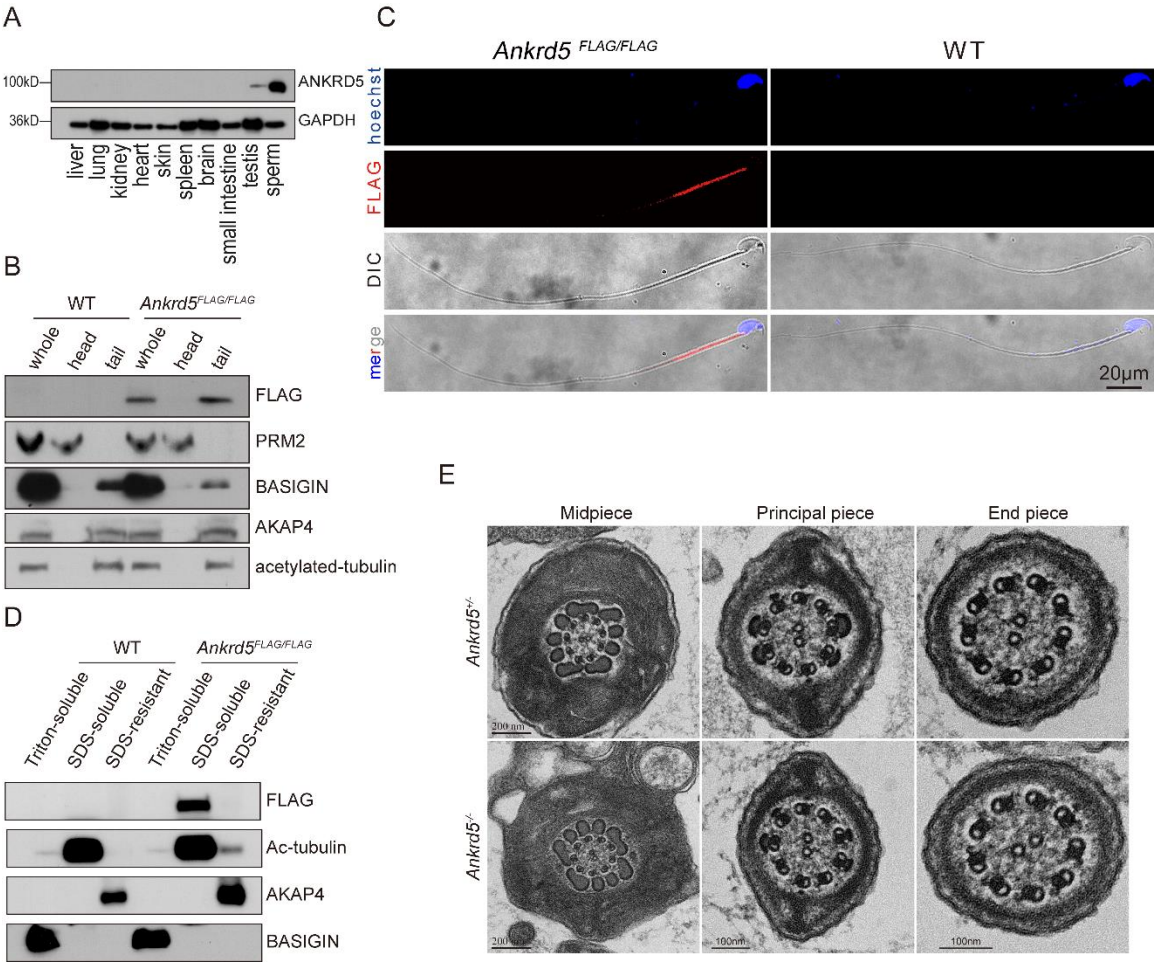

Figure 4. ANKRD5 is located in the midpiece of sperm axoneme. (A) Immunoblotting analysis of various mouse tissues. GAPDH was used as the loading control. (B) Head and tail separation of mouse spermatozoa. ANKRD5-FLAG was detected in the tail fraction. PRM2 was used as a marker for sperm head. BASIGIN, AKAP4 and acetylated tubulin were detected as a marker for tails. (C) Immunofluorescence staining results of spermatozoa from wild-type and ANKRD5-FLAG mouse using anti-FLAG antibody (red: anti-FLAG signal; Hoechst: blue). (D) Fractionation of sperm proteins using different lysis buffers. ANKRD5-FLAG was found in the SDS-soluble fraction that contains axonemal proteins. BASIGIN, acetylated tubulin, and AKAP4 were detected as a marker for Triton-soluble, SDS-soluble, and SDS-resistant fractions, respectively. (E) Ultrastructure of sperm tails in control and *Ankrd5* KO mouse. Cross-sections of midpiece, principal piece and end piece were observed using transmission electron microscopy.

A

Rank	Accession number	Protein description	Mascot score	MW	Matched queries	Matched peptides
1	IPI00134915	Ankrd5 Ankyrin repeat domain-containing protein 5	1443	86849	40	32
2	IPI00462140	Krt77 Keratin, type II cytoskeletal 1b	268	61322	6	4
3	IPI01008396	Tcte1 T-complex-associated testis-expressed protein 1 *	92	55484	2	2
4	IPI00463886	Gm7429 60S ribosomal protein L30-like	70	12824	2	2
5	IPI00137227	Rab2a Ras-related protein Rab-2A	65	23533	3	2
6	IPI00467880	Lrrc48 Uncharacterized protein *	64	23771	1	1
7	IPI00323130	Tceb1;LOC100045866 Transcription elongation factor B polypeptide 1	63	12465	1	1
8	IPI00420988	Ccdc135 Isoform 1 of Coiled-coil domain-containing protein 135 *	58	103145	2	2
		⋮				
165	IPI00120312	Gas8 Growth arrest-specific protein 8 *	21	56229	1	1

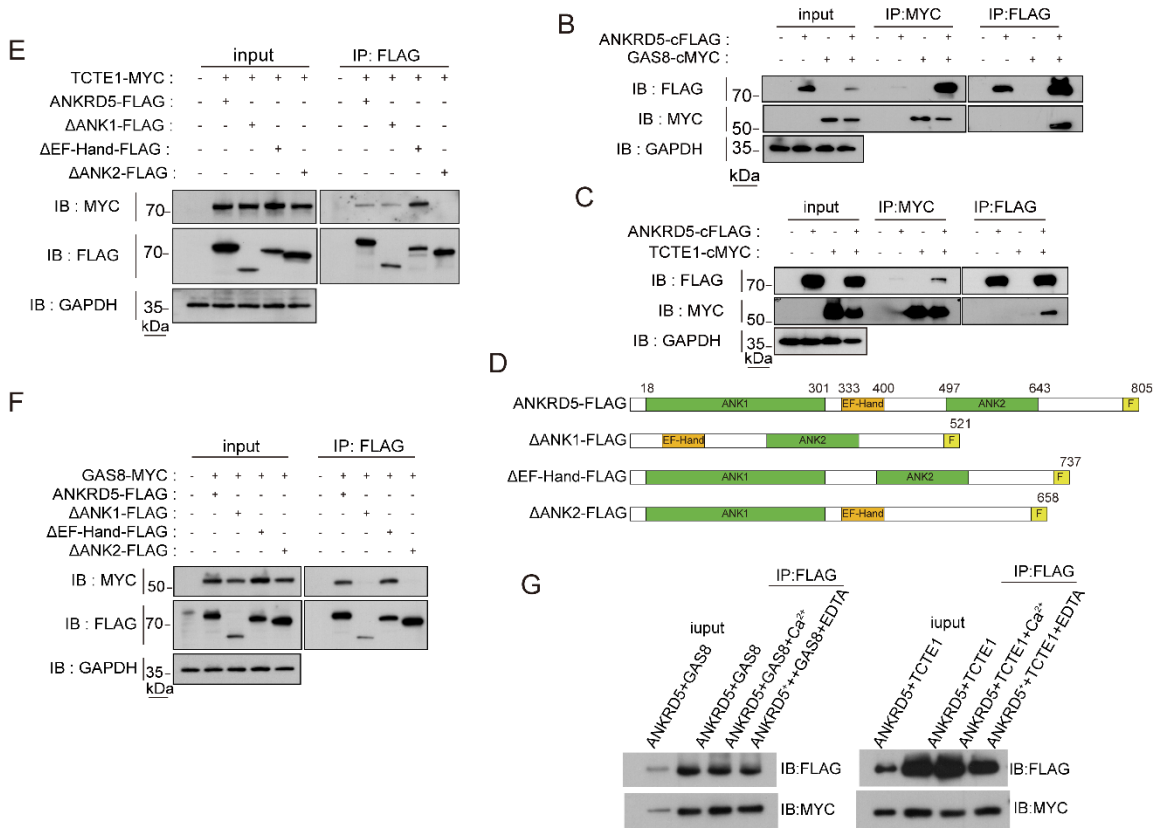

Figure 5. ANKRD5 is a component of N-DRC in sperm flagella. (A) Identification of sperm proteins in LC-MS/MS analysis. Black star indicates N-DRC components. (B and C) Individual DRC components were coexpressed in HEK293T cells. Immunoprecipitation of ANKRD5-FLAG resulted in the co-precipitation of GAS8-MYC and TCTE1-MYC. Similarly, immunoprecipitation of GAS8-MYC and TCTE1-MYC also led to the co-precipitation of ANKRD5-FLAG. (D) Schematic of various truncated ANKRD5 vectors. FLAG-tag was linked posterior to the C-terminal of ANKRD5. Green and yellow boxes show the ANK domain and EF-Hand domain of ANKRD5, respectively. Light yellow boxes indicate FLAG tag. (E and F) The interaction between various truncated ANKRD5-FLAG and TCTE1-MYC or GAS8-MYC were confirmed by co-IP followed by WB analysis using anti-FLAG, and anti-MYC antibodies. (G) Effect of calcium ion and EDTA treatment on the interaction of ANKRD5 with GAS8 and TCTE1.

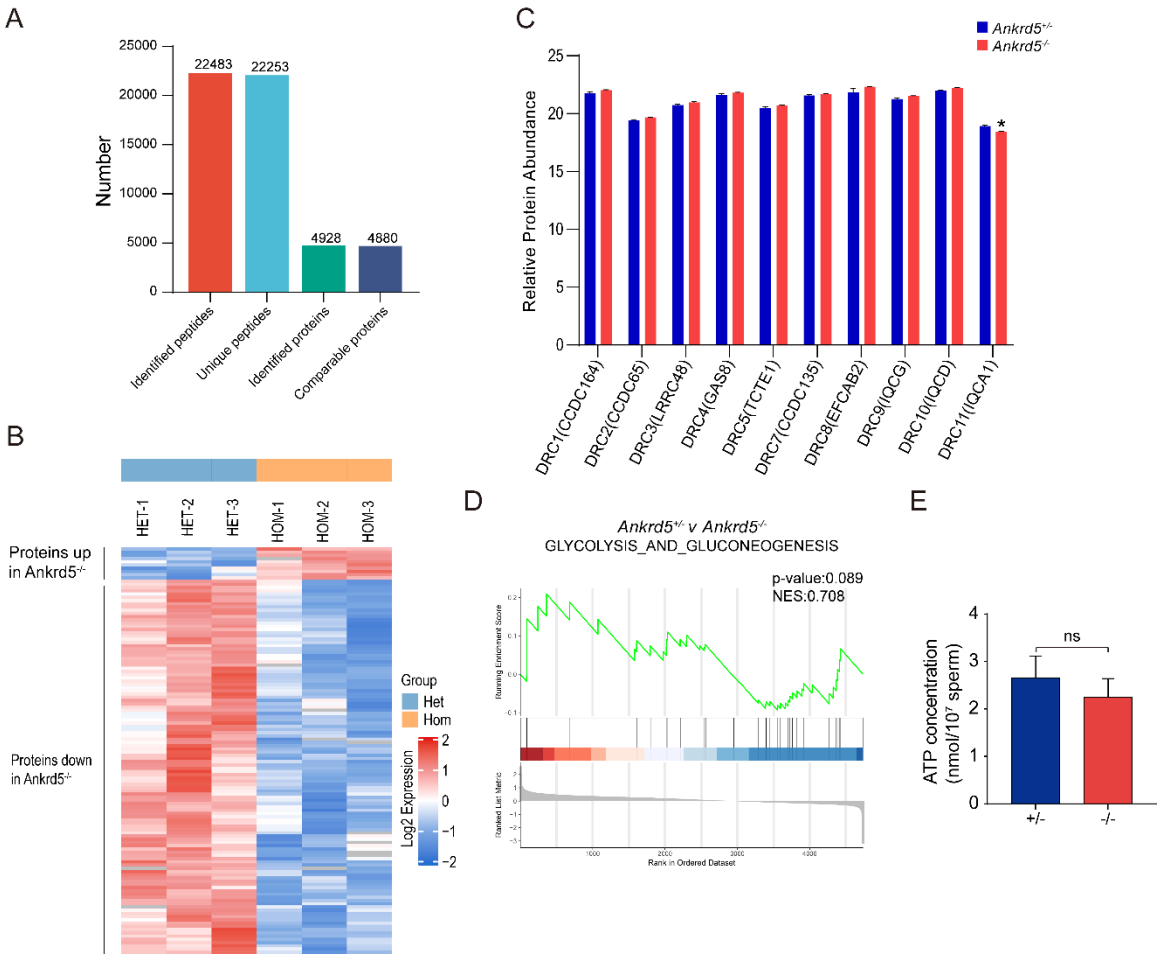

Figure 6. Absence of ANKRD5 does not affect energy metabolism. (A) The differentially expressed proteins of *Ankrd5*$^{+/-}$ and *Ankrd5*$^{+/-}$ were identified by 4D-SmartDIA. (B) Heatmap of relative protein abundance changes between control and knockout mouse sperm. (C) Differences in the expression of N-DRC protein components identified by mass spectra. *P < 0.05, Student's t test; error bars represent SE (n = 3). (D) GSEA analysis of glycolysis and gluconeogenesis. (E) Measured levels of ATP between wild-type and *Ankrd5* null sperm. Student's t test; error bars represent SE (n = 3).

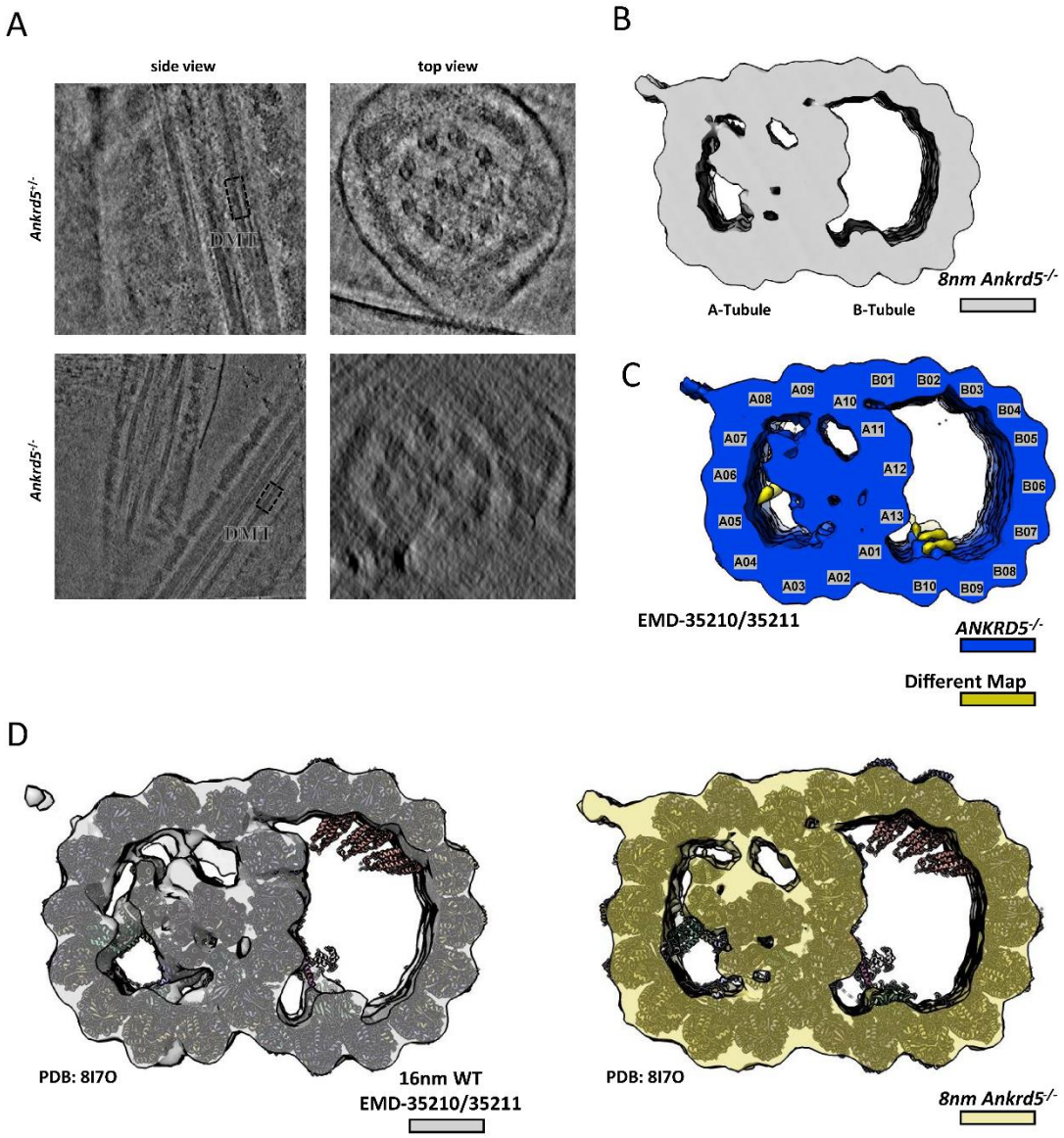

Figure 7. The overall structure of *Ankrd5*-KO mouse sperm DMT. (A) Side view and top sectional view of WT/*Ankrd5*$^{-/-}$ mouse sperm axoneme are shown in the tomogram slices. (B) The cryo-EM map of *Ankrd5*$^{-/-}$ mouse sperm DMT with an 8 nm repeat was obtained by sub-tomogram analysis. (C) Loss of density in *Ankrd5*$^{-/-}$ DMT structure. The transverse sectional view of DMT is shown. The lost density (khaki color) was obtained by subtracting the density map of *Ankrd5*$^{-/-}$ DMT from that of the WT DMT. (D) The model of 16nm-repeats WT DMT (PDB: 8I7O) was fitted in the 16nm repeat WT DMT map and *Ankrd5*$^{-/-}$ DMT map.

A

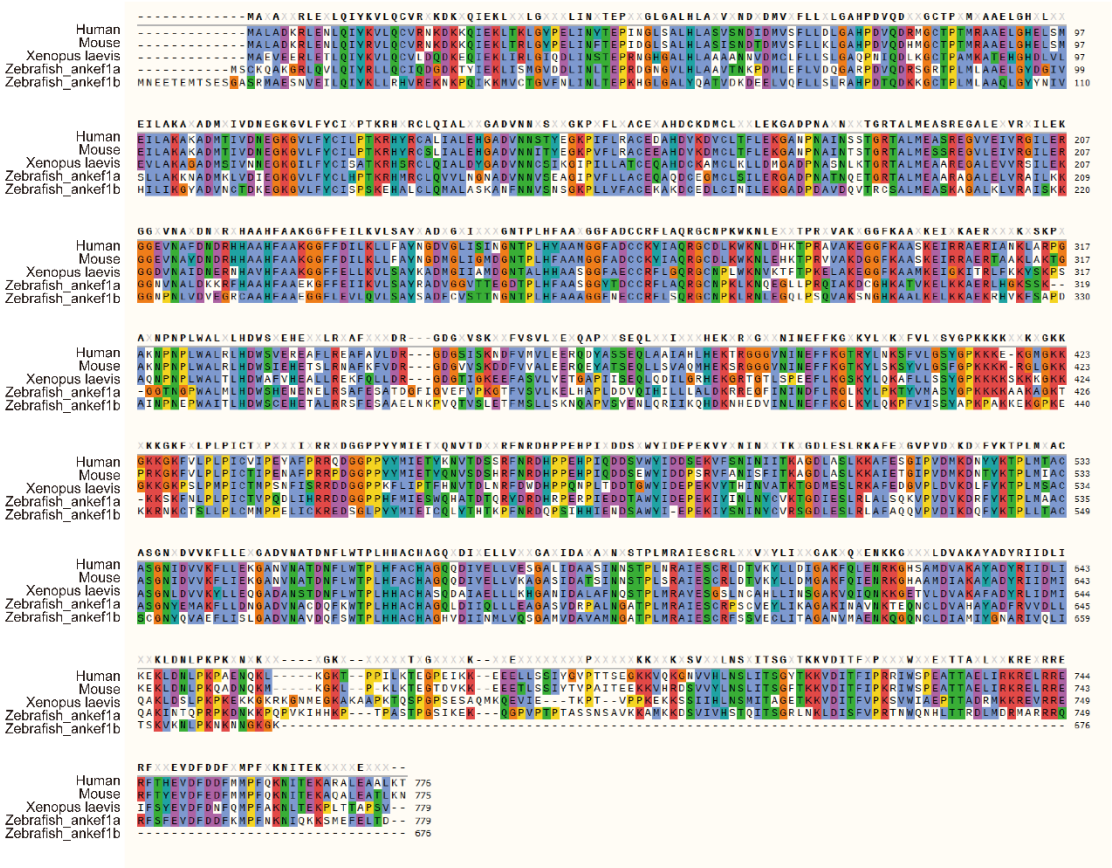

B

Percent Identity

	1	2	3	4	5		
1		85.42	58.09	50.19	48.71	1	Human
2	85.42		57.42	50.46	47.04	2	Mouse
3	58.09	57.42		52.21	46.67	3	Xenopus
4	50.19	50.46	52.21		54.16	4	Zebrafish 1a
5	48.71	47.04	46.67	54.16		5	Zebrafish 1b
	1	2	3	4	5		

Percent Divergence

C

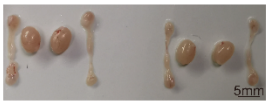

D

Figure S1. ANKRD5 is conserved between human and other vertebrate model organisms. (A) Sequence alignment of ANKRD5 proteins from several species. Sequences were derived from NCBI and compared with SnapGene (Version=4.3.6). (B) Percent identity matrices of *Ankrd5* proteins across several common vertebrate model organisms. (C) Gross morphology of adult control and *Ankrd5* KO testes and epididymis. (D) The body size was similar between *Ankrd5*$^{+/-}$ and *Ankrd5*$^{-/-}$ mice.

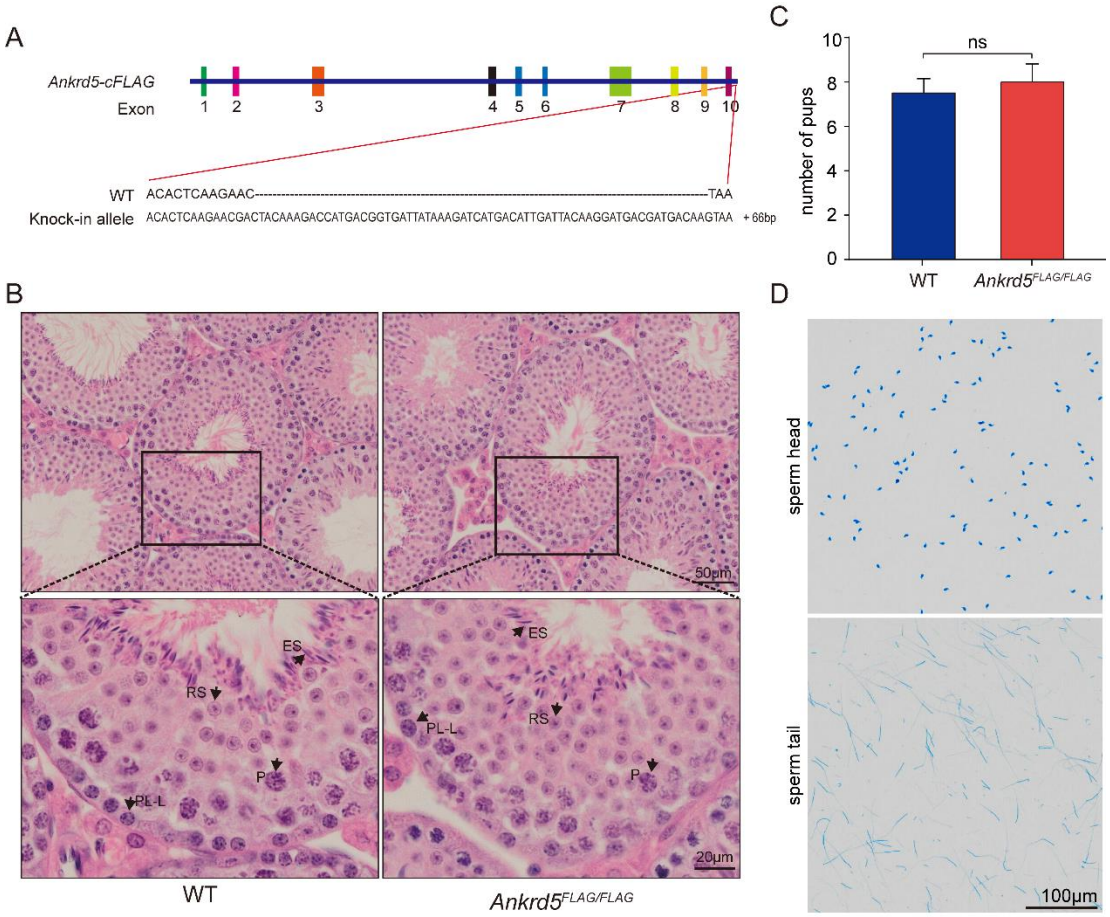

Figure S2. The generation of FLAG-tagged mouse and sperm head and tail separation. Schematic of FLAG-tagged alleles of endogenous *Ankrd5* generated using CRISPR/Cas9. (B) Hematoxylin and eosin (H&E) staining of FLAG-tagged mouse testis. No overt abnormalities were found. P, pachytene; ES, elongated sperm; RS, round sperm; SG, spermatogonia; ST, Sertoli cell. (C) There was no significant difference in litter size between WT and FLAG-tagged mouse. Values represent mean ± SE (n=3). (D) Sperm head and tail were separated by repeated freeze-thaw and stained with Coomassie Brilliant Blue R-250.

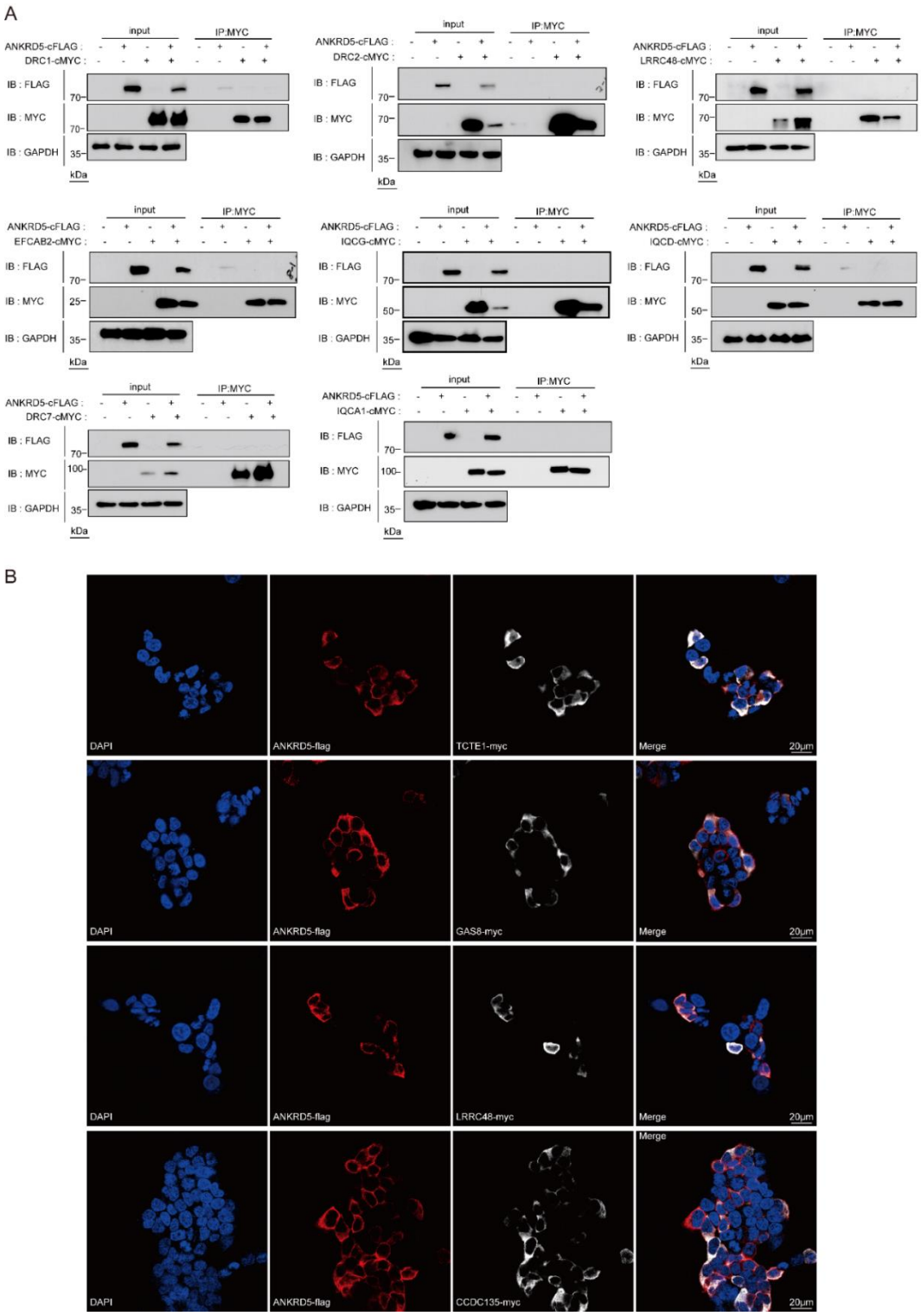

Figure S3. Identify the interaction of ANKRD5 and other N-DRC components. (A) Co-IP followed by WB analysis were performed using lysates collected from HEK293T cells transfected with FLAG tagged ANKRD5. Immunoprecipitated proteins by anti-MYC antibody were analyzed by WB using anti-FLAG antibodies. (B) HEK293T cells transiently expressing ANKRD5-FLAG and DRC-MYC were stained with FLAG (red) and MYC (white) to visualize ANKRD5 and DRC, respectively. DAPI (blue) was used to visualize the nuclei.

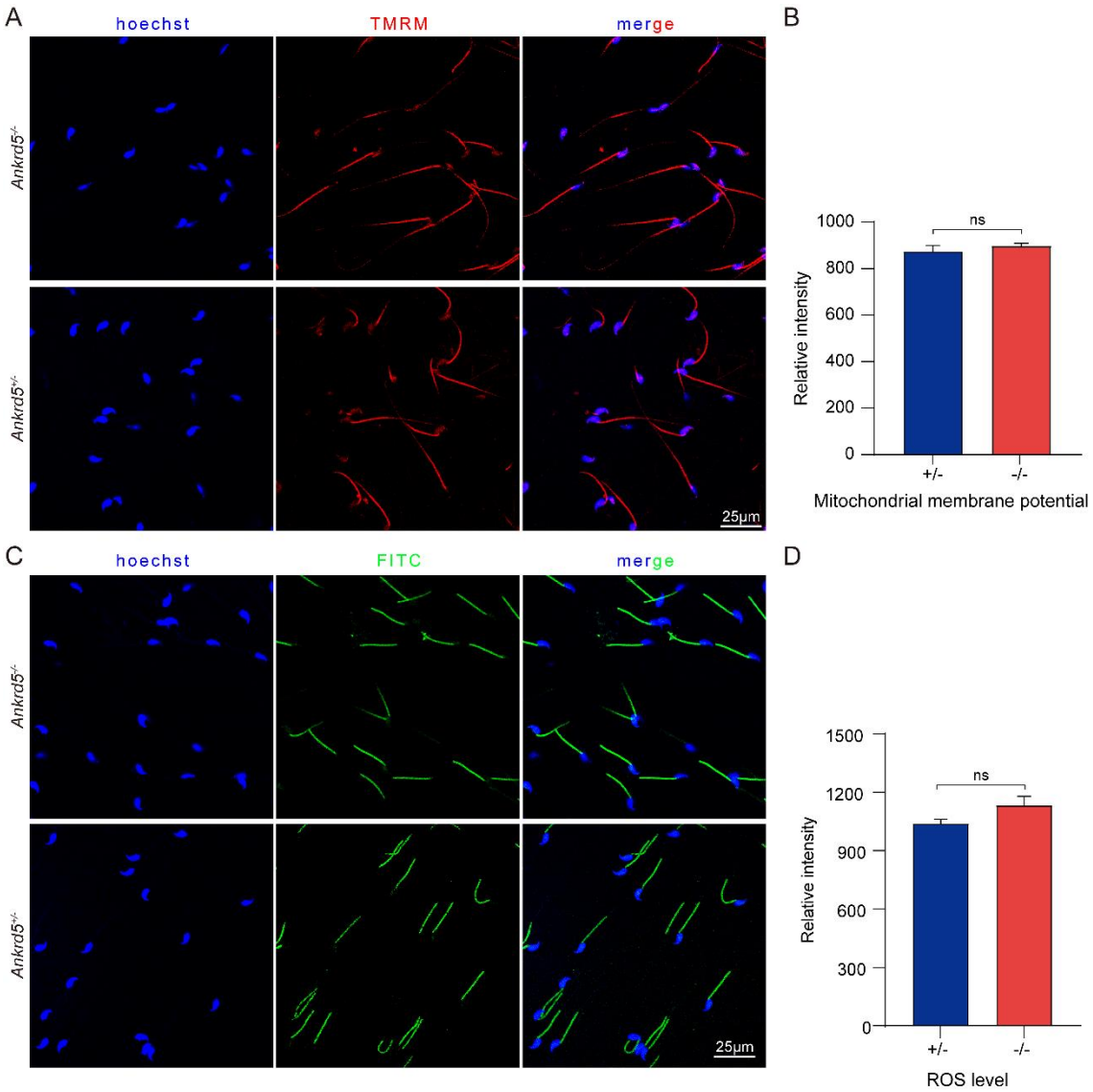

Figure S4. The mitochondrial membrane potential and ROS levels of *Ankrd5* null sperm was normal. (A) Mitochondrial activities assessed by fluorescence of TMRM, RFP filter. The higher the potential, the higher the concentration of TMRM in mitochondria, resulting in an increased fluorescence intensity. (B) Graphs show semi-quantitative of TMRM fluorescence intensity. Values represent mean ± SE (n=3). (C) ROS levels assessed by fluorescence of DCFH-DA, FITC filter. The higher the concentration of ROS, the higher fluorescence intensity. (D) Graphs show semi-quantitative of FITC fluorescence intensity. Values represent mean ± SE (n=3).

A

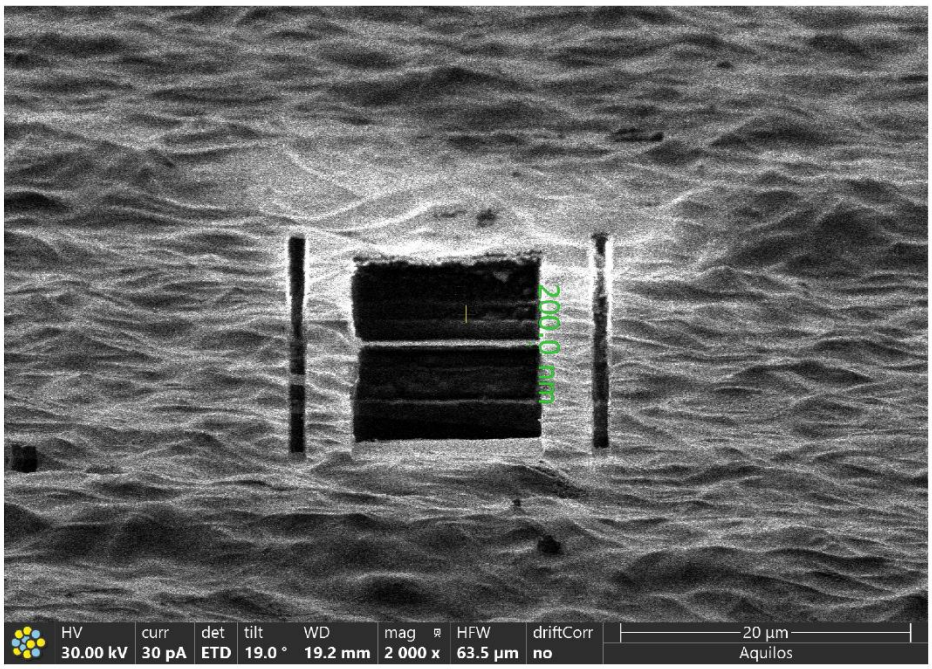

B

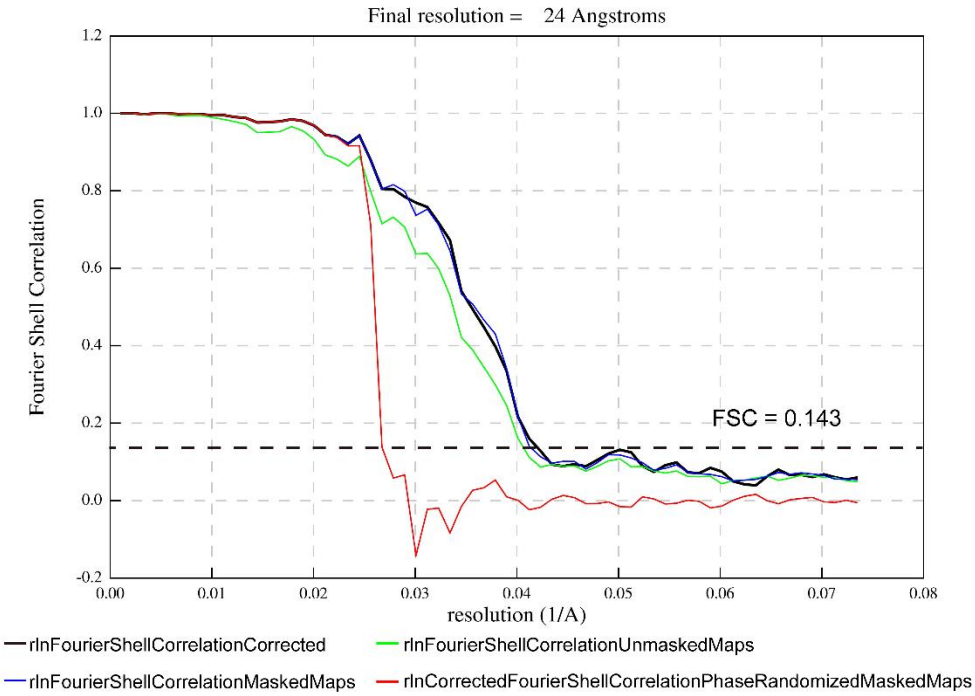

Figure S5. Cryo-FIB milling and the half-map Fourier Shell Correlation (FSC) of the *Ankrd5*$^{-/-}$ mouse sperm axoneme. (A) Inspection of frozen sperm on the grid after FIB milling. The thin lamellae were used for data collection. (B) The half-map Fourier Shell Correlation (FSC) plot of *Ankrd5*$^{-/-}$ DMT is shown.

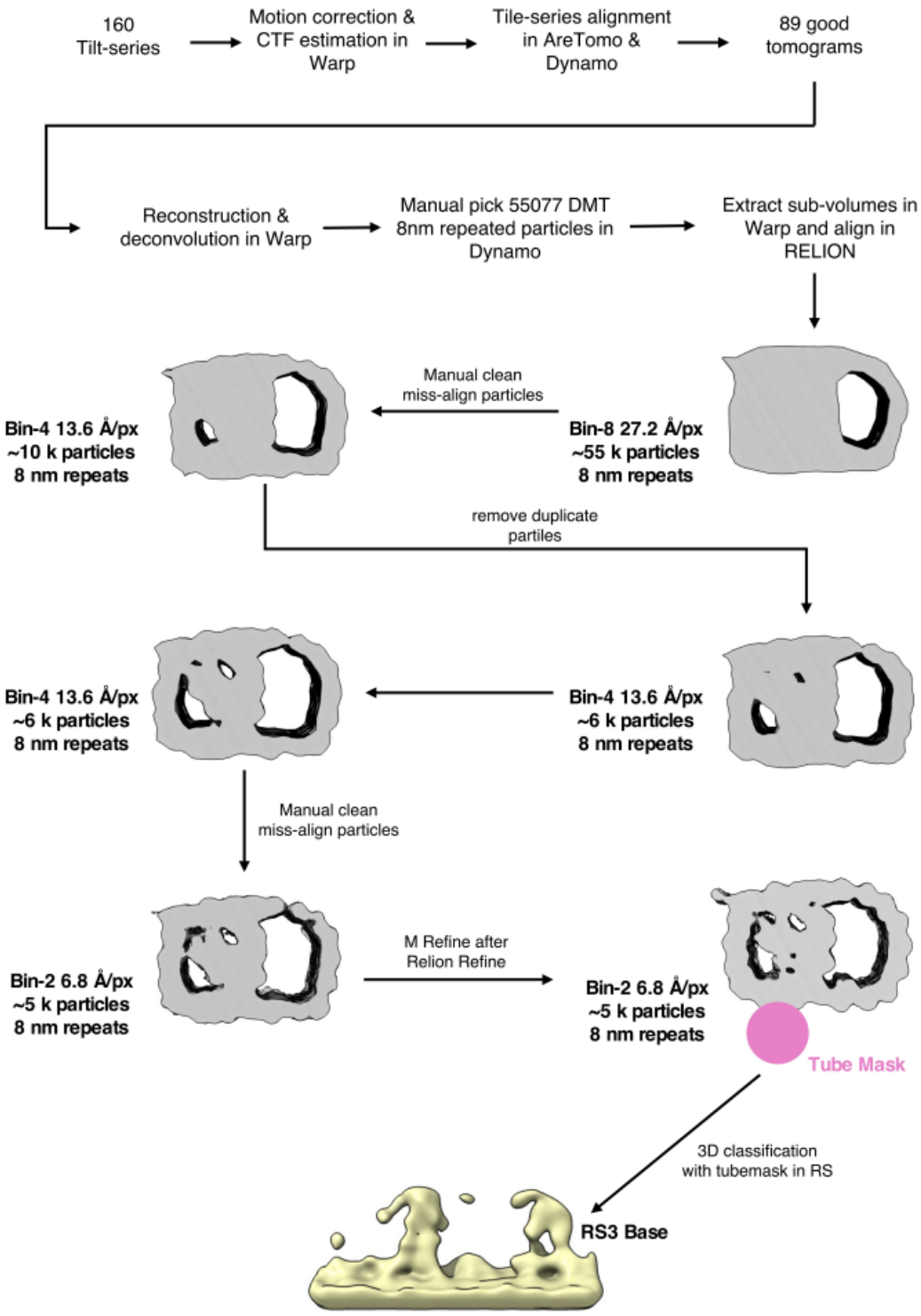

Figure S6. The data processing of ANKRD5-KO mouse sperm DMT. The pixel sizes at different binning levels are indicated in angstroms per pixel (Å/px for short).

Movie S1. Sperm from *Ankrd5*$^{+/-}$ mouse. Video recording of sperm from *Ankrd5*$^{+/-}$ mouse from the Computer Assisted Sperm Analyzer system (Version.12 CEROS, Hamilton Thorne Research). Capture rate was set at 60 frames/second.

Movie S2. Sperm from *Ankrd5*$^{-/-}$ mouse. Video recording of sperm from *Ankrd5*$^{-/-}$ mouse from the Computer Assisted Sperm Analyzer system (Version.12 CEROS, Hamilton Thorne Research). Capture rate was set at 60 frames/second.

Table_1

Knockout of *Ankrd5* causes male infertility of mouse Male mouse

	Females	Plugs	Litters	Mean litter size
WT (n=6)	12	11	10	8
Ankrd5 $^{+/-}$ (n=6)	12	12	10	8.5
Ankrd5 $^{-/-}$ (n=6)	12	10	0	0